



Deposited via The University of Leeds.

White Rose Research Online URL for this paper:

<https://eprints.whiterose.ac.uk/id/eprint/142779/>

Version: Accepted Version

Article:

Walowski, KJ, Kirstein, LA, De Hoog, JCM et al. (2019) Investigating ocean island mantle source heterogeneity with boron isotopes in melt inclusions. *Earth and Planetary Science Letters*, 508. pp. 97-108. ISSN: 0012-821X

<https://doi.org/10.1016/j.epsl.2018.12.005>

© 2018 Elsevier B.V. Licensed under the Creative Commons Attribution-NonCommercial-NoDerivatives 4.0 International License
(<http://creativecommons.org/licenses/by-nc-nd/4.0/>).

Reuse

This article is distributed under the terms of the Creative Commons Attribution-NonCommercial-NoDerivs (CC BY-NC-ND) licence. This licence only allows you to download this work and share it with others as long as you credit the authors, but you can't change the article in any way or use it commercially. More information and the full terms of the licence here: <https://creativecommons.org/licenses/>

Takedown

If you consider content in White Rose Research Online to be in breach of UK law, please notify us by emailing eprints@whiterose.ac.uk including the URL of the record and the reason for the withdrawal request.



1 **Investigating ocean island mantle source heterogeneity with boron isotopes in melt**
2 **inclusions**

3

4 Walowski, K.J.^{1,2*}, Kirstein, L.A.¹, De Hoog, J.C.M.¹, Elliot, T.³, Savov, I.P.⁴, Jones,
5 R.E.⁵, EIMF⁶

6

7 ¹ University of Edinburgh, School of Geosciences, Grant Institute, Edinburgh, UK

8 ² Middlebury College, Department of Geology, Middlebury, VT, USA

9 ³ University of Bristol, School of Earth Sciences, Bristol, UK

10 ⁴ University of Leeds, School of Earth and Environment, Leeds, UK

11 ⁵ University of Oxford, Department of Earth Sciences, Oxford, UK

12 ⁶ Edinburgh Ion Microprobe Facility, Grant Institute, University of Edinburgh,
13 Edinburgh, UK

14

15 *Corresponding Author - Current contact information: kwalowski@middlebury.edu

16

17 Keywords: Ocean island basalts; Mantle Volatiles; Mantle Geochemistry; Boron

18 Isotopes; Melt inclusions; Geochemistry; Volatile Recycling

19

20 **Abstract**

21 Recycling of the lithosphere via subduction drives the trace element and isotopic
22 heterogeneity of the mantle, yet, the inventory of volatile elements in the diverse array of
23 mantle reservoirs sampled at ocean islands remains uncertain. Boron is an ideal tracer of

24 volatile recycling because it behaves similarly to volatiles during high-temperature
25 geochemical reactions and carries a distinctive isotope signature into the mantle, but is
26 subsequently little-influenced by degassing on return to the surface. Furthermore, B-rich
27 recycled lithologies will have a strong influence on typical upper mantle compositions
28 characterized by low B concentrations ($<0.2 \mu\text{g/g}$ and $\delta^{11}\text{B} -7.1\pm 0.9\text{‰}$). Here, we present
29 and compare the B abundances and isotope compositions, together with the volatile
30 element contents (H_2O , CO_2 , and Cl) of basaltic glasses and olivine-hosted melt
31 inclusions from two different ocean island localities (La Palma, Canary Islands, and Piton
32 de Caille, La Réunion Island). Our results suggest that olivine hosted melt inclusions are
33 protected from contamination during ascent and provide more robust estimates of
34 primary mantle source $\delta^{11}\text{B}$ than previous bulk rock studies. We find that the $\delta^{11}\text{B}$ of the
35 La Réunion samples ($-7.9\pm 0.5\text{‰}$ (2σ)) overlaps with the recently defined MORB datum,
36 indicating that the depleted upper-mantle and ‘primitive mantle’ reservoirs are
37 indistinguishable with respect to $\delta^{11}\text{B}$, or that B concentrations are sufficiently low that
38 they are diluted by partial melting in the uppermost mantle. In contrast, the La Palma
39 samples, notable for their radiogenic Pb isotope ratios, are characterized by $\delta^{11}\text{B}$ values
40 that are distinctly isotopically lighter ($-10.5\pm 0.7\text{‰}$ (2σ)) than La Réunion or MORB. We
41 suggest these isotopically light values are derived from significantly dehydrated recycled
42 materials preserved in the La Palma mantle source region, in keeping with their lower
43 B/Zr and $\text{H}_2\text{O}/\text{Ce}$. This work therefore provides strong new support for subduction zone
44 processing as a mechanism for generating radiogenic Pb isotopic signatures and volatiles
45 heterogeneities in the mantle.

46

47 **1. Introduction**

48 Physical and chemical interactions between the mantle and the Earth's surface
49 have controlled the long-term evolution of the crust, the oceans, and the atmosphere. The
50 mantle is a potentially major reservoir of the volatile elements, which in turn can have a
51 major effect on the physical properties the Earth's interior (e.g., Jung and Karato, 2001).
52 Yet, the volatile element composition of the Earth's interior remains poorly
53 characterized. Tectonic recycling of oceanic lithosphere, specifically, is a key control of
54 the volatile element distribution in the Earth's interior and is also thought to have
55 generated mantle heterogeneity throughout Earth's history for a range of other elements
56 (e.g. Allègre 1982, Hofmann and White, 1982). Indeed, our understanding of the
57 influence of subducted recycled material on mantle composition, reflected in
58 compositional variability in ocean island basalts (OIB) and to a lesser extent mid-ocean
59 ridge basalt (MORB), remains largely supported by the initial observations made in the
60 early 1980s based on the modest selection of isotope systems (Sr, Nd, Pb) that could be
61 measured with sufficient precision at the time (e.g., Zindler and Hart, 1986). Subsequent
62 work utilizing other stable isotope systems such as O, Fe, Li, Mg, U, Tl and Cl isotopes
63 have provided continued support for recycling of surficial materials into the deep mantle
64 (e.g., Eiler et al., 1997; Turner et al., 1997; Ryan and Kyle, 2004; Teng et al., 2010,
65 Nielson et al., 2006; Williams and Bizimis, 2014) but, the origin of various indices of
66 source heterogeneity continue to be debated.

67 An important step forward would be to link mantle heterogeneities with volatile
68 elements that intrinsically represent a distinct part of the recycling process. However, the
69 volatile character and composition of different mantle end-members remains poorly

70 understood. Recent work from Dixon et al. (2017) utilizing enriched MORB
71 compositions provides initial evidence that volatiles and their light stable isotopes,
72 primarily δD , may become decoupled from other lithophile elements through a complex
73 multistage dehydration and re-equilibration journey of subducting slabs from the surface
74 to the transition zone.

75 A perfect tracer for slab recycling should be only fractionated at the Earth's
76 surface, have a strong influence on mantle compositions but be resistant to perturbations
77 en route back to the surface, all of which apply to B (De Hoog and Savov, 2018). Boron
78 is strongly enriched and isotopically fractionated in altered oceanic crust (e.g., Smith et
79 al., 1995; Nakamura et al., 1992), serpentinized oceanic lithospheric mantle (e.g., Pabst et
80 al., 2012; Harvey et al., 2014), and sediments (e.g., Ishikawa and Nakamura, 1993;
81 Tonarini et al., 2011; *for a detailed data compilation see Marschall, 2018 and references*
82 *there within*). The mantle is strongly depleted in B due to its relatively incompatible
83 nature (similar to LREE; Ryan et al., 1996; Ishikawa & Tera, 1999; Marschall et al.,
84 2017) and so, recycled slab materials, where and if present, should have a significant
85 impact on mantle B abundances and their isotopic makeup (Marschall et al., 2018). Thus,
86 B isotopes have the potential to track the fate of recycled lithosphere, which may also be
87 a major repository of water, halogens and noble gases in the deep mantle (Kendrick et al.,
88 2012).

89 A number of studies have employed boron concentrations and isotope ratios in an
90 attempt to characterize recycled components in OIB mantle sources (e.g., Ryan et al.,
91 1996; Chaussidon and Marty, 1995, Gurenko and Chaussidon, 1997). However, the data
92 interpretation of these previous studies suffered from a poorly-defined baseline for

93 MORB and DMM, and inclusion of samples that had assimilated hydrothermally altered
94 materials (see Marschall et al., 2017), or inadequate analytical precision. In this study, we
95 build upon recent improvements to the in-situ analytical techniques for measuring $\delta^{11}\text{B}$ in
96 low boron concentration samples (e.g., Marschall and Monteleone, 2015), including the
97 improved characterization of glassy reference materials (e.g., Rosner and Meixner, 2004)
98 and contrast new measurements against a comprehensive reassessment of the $\delta^{11}\text{B}$
99 variability within a global MORB dataset (Marschall et al., 2017).

100 To test the capabilities of B isotopes as a tracer for recycled oceanic crust, here,
101 we compare contrasting OIBs from La Réunion Island with high He^3/He^4 (Hanan &
102 Graham, 1996), elevated $^{207}\text{Pb}/^{204}\text{Pb}$ and old model ages (Chase, 1981), possibly Hadean
103 (Peters et al., 2018), to those from La Palma which display radiogenic Pb and trend
104 toward the so-called HIMU end-member (“high μ ” where $\mu = ^{238}\text{U}/^{204}\text{Pb}$; Zindler and
105 Hart, 1986). The mantle source of the La Réunion magmas thus represents a ‘primitive
106 mantle’ composition, potentially little modified over Earth’s history (comparable to the
107 ‘primitive helium mantle’ or ‘the common mantle component;’ Farley et al., 1992 and
108 Hanan and Graham, 1996, respectively). Conversely, the HIMU end-member,
109 characterized by elevated $^{206}\text{Pb}/^{204}\text{Pb}$ ratios at low $^{87}\text{Sr}/^{86}\text{Sr}$ ratios, is consistently
110 suggested to be formed, in part, by recycled ancient subduction-modified crust (Fig. 1;
111 Chauvel et al., 1992; Marcantonio et al., 1996; Day et al., 2010). A key aspect of this
112 study is that we have analyzed melt inclusions. The necessity for this is two-fold: (1)
113 olivine host-phenocrysts can shield the sample from crustal and seawater
114 contamination/assimilation which may overprint the $\delta^{11}\text{B}$ of the mantle source (Rosner et
115 al., 2004; 2008; Gurenko & Kamenetsky, 2011), and (2) melt inclusions provide the best

116 estimates of initial volatile concentrations which can be utilized to infer mantle source
117 volatile concentrations (e.g., Michael et al., 1995) as well as minimum estimates of
118 crystallization depths (e.g., Newman and Lowenstern, 2000). Despite the potential for
119 various post-entrapment modification processes in melt inclusions (Wallace et al., 2015
120 and references there within), our study focuses on the most valuable, rapidly quenched
121 samples (i.e. loose olivine from the coarse-ash sized fraction of a tephra deposit, as
122 opposed to olivine phenocrysts found within a thick, slowly cooled lava flow or larger
123 scoria clasts/bombs; e.g., Lloyd et al., 2013) and employs well-established post-
124 entrapment crystallization corrections (e.g., Danyushevsky et al., 2002; Lloyd et al.,
125 2013; Wallace et al., 2015) to determine the best estimates of pre-eruptive volatiles
126 possible.

127 Hence, we aim to re-examine how two different deep mantle sources compare in
128 their $\delta^{11}\text{B}$ system to MORB, and determine the volatile (H_2O , CO_2 , Cl, and F)
129 composition of basaltic melt inclusions to better understand the concentrations and
130 distribution of volatiles in deep recycled mantle material.

131

132 **2. Sample Locations and Descriptions**

133

134 **2.1 Piton de Caille, Piton de la Fournaise, Réunion Island**

135 Piton de la Fournaise is one of the most active hotspot volcanoes on Earth, and
136 represents the most recent expression of a long-lived mantle plume which previously
137 formed the Deccan Traps (65 Ma; Albarède, 1997 and reference there within). The island
138 is situated on oceanic crust that is ~64 Ma, and typically erupts transitional aphyric

139 basalts and picritic basalts along fissures, although more explosive Strombolian activity
140 also produces fire-fountaining and builds scoria cones. Piton de Caille represents one
141 such scoria cone found in the NW rift zone that erupted <5000 years ago (Bureau et al.,
142 1998). In this study, we have acquired samples of wind-sorted olivine-rich material
143 derived from the Piton de Caille vent. The olivine phenocrysts from this sample are large
144 (1-5mm) and contain numerous large glassy melt inclusions.

145 Primitive magmas erupted from Piton de la Fournaise are generally characterized
146 by tholeiitic compositions (e.g., Albarède, 1997) and are thought to be derived from
147 mantle with elevated potential temperatures indicative of a deep-seated plume source
148 (e.g., Sobolev and Nikogosian, 1994). In addition, a restricted range of $^{187}\text{Os}/^{188}\text{Os}$ ratios
149 indicate a relatively homogenous source that has not been significantly affected by
150 oceanic crust and/or continental sediment inputs (Schiano et al., 2012), while high
151 $^3\text{He}/^4\text{He}$ and ^{142}Nd indicate this reservoir has potentially been isolated from significant
152 mantle mixing since the Hadean (Peters et al., 2018). These numerous characteristics
153 provides a basis for the sample choice as an example of an OIB that represents melting of
154 relatively undisturbed and deeply sourced primitive mantle.

155

156 **2.1 La Palma, The Canary Archipelago**

157 The Canary Archipelago, located offshore NW Africa, is a westward-younging
158 volcanic island chain suggested to be the result of a low buoyancy or weak mantle plume
159 impinging beneath the African plate (Schminke, 1982). La Palma is one of the most
160 recently active island in the Canaries, still in its shield building phase and is built on
161 oceanic crust ~160 Ma in age. Magmas erupted at La Palma are highly silica-

162 undersaturated, befitting its position atop thick lithosphere (e.g., McBirney and Gass,
163 1967). La Palma lavas have radiogenic Pb isotopic compositions but relatively
164 unradiogenic Sr isotope ratios (Fig. 1), a so-called HIMU affinity, which has been widely
165 interpreted to reflect the contribution of recycled mafic crust (Zindler and Hart 1986).
166 This general inference has been further supported by highly radiogenic Os isotope ratios
167 (Marcantonio et al., 1996) and low $\delta^{18}\text{O}$ (Day et al., 2010). Evidence for a recycled
168 component in the La Palma mantle source and access to appropriate samples thus
169 provides a contrast to the La Réunion samples to test the effectiveness of boron isotopes
170 in tracking recycled material in OIB mantle sources.

171 La Palma additionally provides a wealth of young, explosive cone deposits from
172 which to collect samples for melt inclusion work. The island is comprised of two main
173 edifices, the extinct ~1 Ma Taburiente Shield in the north, and the historically active
174 Cumbre Vieja Ridge (Hernandez-Pacheco and Valls, 1982). Samples for this study were
175 acquired from both edifices. From Taburiente, two scoria samples were collected from a
176 relict cone interbedded in a ~0.7 Ma continuous lava sequence exposed in the Barranco
177 Fagundo (Fig. 2; Supplementary Table TS1), the locality from which previous studies
178 measured the highest Pb isotope ratios (Nikogosian et al., 2002). From the Cumbre Vieja
179 Ridge, coarse-ash was sampled from a road-cut Holocene-age cone at the northernmost
180 extension of the Cumbre Vieja Ridge, and from the 1949 eruption of Vólcan Duraznero
181 (Fig. 2; Supplementary Table TS1). A detailed description of sample localities is
182 provided in Supplementary Table TS1.

183

184 **3. Methods**

185 **3.1 Sample preparation and analytical methods**

186 All samples analyzed in this study are derived from the coarse-ash size fraction of
187 tephra deposits. This type of material was collected to obtained naturally quenched
188 inclusions in order to minimize the potential for syn-eruptive diffusive loss of volatile
189 elements (e.g., hydrogen; Lloyd et al., 2013) or crystallization of melt inclusions.
190 Individual loose olivine phenocrysts (250 μm to 2 mm in length) were hand-picked from
191 sieved tephra and examined in immersion oils or alcohol to locate the melt inclusions.
192 Olivine crystals hosting fully enclosed, glassy melt inclusions were mounted in acetone-
193 soluble acrylic resin in 5mm diameter aluminum rounds and individually polished to
194 expose melt inclusions. Polished olivine phenocrysts hosting melt inclusions were then
195 removed from the acrylic resin following a 3-step treatment in acetone and subsequently
196 remounted in epoxy resin mounts. The final epoxy mounts were polished, cleaned and
197 coated in Au.

198 The samples were first analyzed for boron isotope ratios ($\delta^{11}\text{B}$) using the Cameca
199 IMS-1270 secondary ion mass spectrometer at the NERC Edinburgh Ion Microprobe
200 Facility (EIMF). The uncertainties of the measurements were typically ca. 1.0‰ (1s) for
201 B concentrations of 1-3 ppm, whereas the accuracy is estimated as 0.9‰ based on the
202 average deviation of calibration standards from their reference values (see Supplementary
203 Materials, Section 1. Analytical Methodology, for details). Following B-isotope analyses,
204 volatile (H_2O , CO_2 , Cl, and F) and selected trace elements (Rb, Sr, Y, Zr, Nb, Ba, La, and
205 Ce) were analyzed in the same melt inclusions using a Cameca IMS-4f SIMS at EIMF
206 using separate analytical routines for CO_2 and all remaining elements. Lastly, melt
207 inclusions and host olivine were analyzed for major elements on the Cameca SX-100

208 electron microprobe at the University of Edinburgh. A complete description of all
209 analytical methods is provided in the Supplementary Materials (Section 1. Analytical
210 Methodology), while additional details of calibrations and reproducibility of $\delta^{11}\text{B}$
211 analyses can be found in Supplementary Table TS4 and TS5.

212

213 **3.2 Melt inclusion corrections**

214 Samples used in this study provided olivine phenocrysts hosting fully-enclosed
215 glassy melt inclusions. However, it is well-known that even the most pristine melt
216 inclusions may have been modified after entrapment (e.g., Esposito et al., 2011; Gaetani
217 et al., 2012). Melt inclusions are typically affected by crystallization of olivine along the
218 walls of the inclusion and by Fe diffusive loss during the time between trapping and
219 eruption (post-entrapment crystallization; PEC; Danyushevsky et al., 2000). The major
220 element compositions of the inclusions were corrected for this PEC and Fe-loss using
221 Petrolog 3.1.1.3 (Danyushevsky and Plechov, 2011), using models for olivine-melt
222 equilibria from Putirka et al. (2005) and oxidation state from Borisov and Shapkin
223 (1990). Concentrations of volatiles and trace elements that are incompatible in the olivine
224 hosts were corrected using the Petrolog results for the major elements. Initial Fe-contents
225 were chosen based on the highest value of FeO^{T} for a melt inclusion suite from each
226 sample. An average oxygen fugacity of $\Delta\text{QFM}+0.6$ was used in the Petrolog calculations
227 based on previous average estimates of $f\text{O}_2$ from La Réunion (Brounce et al., 2017).

228

229 **4. Results**

230 **4.1 Major element compositions**

231 *4.1.1 Piton de Caille, La Réunion*

232 From the Piton de Caille sample, 23 olivine phenocrysts hosting glassy melt
233 inclusions were successfully prepared and analyzed. The olivine host crystals vary from
234 Fo₈₁ to Fo₈₆ (Table 1). Corrected melt inclusions (see section 3.2) are basaltic and
235 subalkaline in composition (Supplementary Fig. 1), consistent with previous studies of
236 samples from the same localities (Bureau et al., 1998). The corrected MgO contents range
237 from ~7-11 wt% (Fig. 4; Table 1), and show little correlation with other major elements
238 (i.e., Al₂O₃, Fig. 4) suggesting only minor olivine and clinopyroxene (CPX) fractionation
239 has affected the lowest-MgO melt inclusions. These observations suggest that the
240 analyzed melt inclusions represent relatively primitive mantle melts, and should provide
241 an adequate representation of their mantle source compositions.

242

243 *4.1.2 La Palma Suite*

244 From the La Palma samples, 44 olivine phenocrysts hosting glassy melt inclusions
245 and 3 subaerial glass beads were successfully prepared and analyzed. Of these, 10 melt
246 inclusions and the glass beads were derived from Barranco Fagundo 01 (BF01), 4 melt
247 inclusions from Barranco Fagundo 02 (BF02), 9 from the Holocene cone, and 21 from
248 the 1949 eruption of Vólcan Duraznero (Fig. 1).

249 The sample BF01 contains olivine phenocrysts Fo₈₂ to Fo₈₆ in composition, while
250 BF02 contains distinctly less primitive olivine phenocrysts, Fo₇₆ to Fo₇₉ in composition
251 (Table 1). Corrected melt inclusions from both samples are alkaline basalts, although
252 those from BF01 are more primitive than those from BF02, containing MgO contents of
253 ~10 wt%, compared with ~6 wt% (Table 1; Fig. 3). We also analyzed glass bead samples

254 from BF01 (i.e. glass not contained within olivine crystals) which represent melts that
255 have fractionated relative to associated melt inclusions compositions (Fig. 3). The
256 Holocene cone sample contains olivine phenocrysts ranging in composition from Fo₇₉ to
257 Fo₈₅. Corrected melt inclusions are basaltic in composition and display a large range in
258 MgO contents from ~6-10 wt%. Melt inclusions from the 1949 eruption of Vólcan
259 Duraznero are hosted in olivine phenocrysts ranging in composition from Fo₇₉ to Fo₈₄.
260 Corrected melt inclusions are basaltic in composition and display a range in MgO
261 contents from ~6-10 wt%.

262 Comparing the La Palma samples, we find a negative correlation between MgO
263 and Al₂O₃, which indicates that variability between samples is dominantly the result of
264 CPX and olivine fractionation. The sample BF01 is the most primitive sample,
265 overlapping in composition with the most primary La Palma magmas, as defined by Day
266 et al. (2010). The major element composition of the remainder of the samples have been
267 variably influenced by fractionation of both CPX and olivine.

268

269 **4.2 Volatile and halogen compositions**

270 *4.2.1 Piton de Caille, Réunion*

271 Dissolved H₂O and CO₂ contents of the Piton de Calle melt inclusions, after
272 correction for PEC and Fe-loss, range between 0.87-1.08 wt% and 949-1468 µg/g,
273 respectively. The Cl compositions are also corrected for PEC and range from 172-432
274 µg/g. As shown in Figure 3c, melt inclusions compositions cluster along an open system
275 degassing path calculated using the Sol_Ex software (Witham et al., 2012) assuming
276 initial volatile contents represented by the composition of the highest measured H₂O and

277 CO₂ (1.08 wt% and 14681 μg/g, respectively). A lack of significant variability in H₂O
278 contents suggests that individual melt inclusions suffered little post-entrapment hydrogen
279 loss (Lloyd et al., 2013; Bucholz et al., 2013). Rather, most variability can be explained
280 by differences in the extent of pre-entrapment degassing (e.g., Johnson et al., 2009)
281 and/or post-entrapment loss in CO₂ (e.g., Wallace et al., 2015; Moore et al., 2015).
282 Although it is difficult to determine which of these two processes controls the observed
283 variability in CO₂, it is important to note most melt inclusions analyzed in this study
284 contain a vapor bubble and such bubbles typically contain a substantial fraction (40-90%)
285 of the CO₂ that was initially dissolved in the trapped melt (Wallace et al., 2015; Moore et
286 al., 2015). As such, the CO₂ contents of the melt inclusions are likely underestimates of
287 the original magmatic CO₂ content. Therefore, estimated depths of entrapment calculated
288 using the Sol-Ex software (Witham et al., 2012) represent minimum estimates of
289 crystallization depths of ~7.5 km.

290 Corrected volatile compositions are compared to published data from Piton de
291 Caille (Bureau et al., 1998) and other vents associated with Piton de la Fournaise
292 (Vigouroux et al., 2009). These comparisons show that the Piton de Caille melt inclusions
293 retain higher volatile contents than those from other La Reunion vents (Fig. 3c).

294

295 *4.2.2 La Palma, Canary Islands*

296 Dissolved H₂O and CO₂ contents of La Palma melt inclusions, after correction for
297 PEC and Fe-loss, range between 0.03-1.96 wt% and 0-4303 μg/g, respectively. The Cl
298 compositions are also corrected for PEC and range from 656-1633 μg/g. All samples
299 show greater amounts of scatter than observed in data from Piton de Caille. As shown in

300 Figure 3d, melt inclusions compositions scatter around an open-system degassing path
301 calculated using the Sol_Ex software (Witham et al., 2012) assuming initial volatile
302 contents represented by the composition of the highest measured H₂O and CO₂ melt
303 inclusions from BF01 (1.52 wt% and 4072 µg/g, respectively).

304 Interestingly, data from Vólcan Duraznero appear to show two different open-
305 system degassing paths (one of which originates at ~0.4 wt% H₂O), which may indicate
306 mixing of two magmas stored at different depths. The presence of multiple magma
307 batches is consistent with observations described in Klügel et al., (2005), but here we
308 simply focus on the H₂O-rich population as the best minimum estimate of the pre-
309 eruptive H₂O contents.

310

311 *4.4 Boron concentrations and $\delta^{11}\text{B}$*

312 Boron concentrations of corrected melt inclusions from Réunion have an average
313 of 2.46 ± 0.31 µg/g, while La Palma magmas have concentrations between 1.8-4.7 µg/g
314 (Fig 4a). These values are consistent with previous bulk rock measurements of high-MgO
315 OIB (Ryan et al., 1996).

316 The average $\delta^{11}\text{B}$ of melt inclusions from Réunion is $-7.9 \pm 0.5\%$ (2σ), which
317 overlap within uncertainty of the newly established global MORB value ($-7.1 \pm 0.9\%$
318 Marschall et al., 2017). At La Palma, melt inclusions have $\delta^{11}\text{B}$ that extend to lighter
319 values. The melt inclusions from BF01 have the lightest average, $-10.5 \pm 0.7\%$, while
320 BF02 melt inclusions have an average $\delta^{11}\text{B}$ of $-8.2 \pm 0.7\%$ and BF01 glass beads have an
321 average of $-8.4 \pm 0.6\%$. The Holocene cone and Vólcan Duraznero have averages of -
322 $9.9 \pm 1.1\%$, and $-10 \pm 0.7\%$, respectively.

323 As shown in Figure 4, $\delta^{11}\text{B}$ values do not correlate with B concentrations.
324 Additionally, the $\delta^{11}\text{B}$ values do not display convincing correlations between other major
325 elements or trace element ratios, such as La/Nb. Thus, observed within-sample variation
326 in $\delta^{11}\text{B}$ is likely the result of analytical uncertainty, as opposed to magmatic processes
327 such as fractionation or partial melting, as previously suggested for the B isotope system.

328 Overall, $\delta^{11}\text{B}$ values from La Palma and La Réunion samples in this study overlap
329 with those previously measured in OIB (Fig. 6; Chaussidon and Marty, 1995; Tanaka and
330 Nakamura, 2005; Genske et al., 2014; Brounce et al., 2012), but are notably much more
331 tightly defined. These $\delta^{11}\text{B}$ values are consistently lighter than those found in arcs, like
332 Kamchatka (Ishikawa et al., 2001; De Hoog and Savov, 2018), and overlap with values
333 from arcs where younger, hotter, oceanic crust is being subducted, like the Cascades
334 (Leeman et al., 2004; Savov et al., 2009; Walowski et al., 2016).

335

336 **5. Discussion**

337 **5.1 Crustal assimilation and seawater alteration**

338 Due to the relatively high B abundance and elevated $\delta^{11}\text{B}$ values in seawater (4.5
339 $\mu\text{g/g}$, +39.5‰; Spivak and Edmond, 1987; Foster et al., 2010), minor assimilation (<3%)
340 of seawater, brines, or seawater-altered materials can significantly increase the B contents
341 and the $\delta^{11}\text{B}$ of the otherwise low-boron basaltic melt (Ryan et al., 1996; Marschall et al.,
342 2017). Thus, identifying the possible influence of assimilation is essential for determining
343 the correct composition of the mantle source region for OIB.

344 Our primary use of melt inclusions decreases the potential for assimilation of
345 seawater-altered materials. The melt inclusions should be armored against contamination

346 post-entrapment and so it is useful to estimate the depth at which this occurs. It is well-
347 established that the ratio of H₂O/CO₂ dissolved in silicate melts is sensitive to pressure
348 (e.g., Newman and Lowenstern, 2002). Despite uncertainty that melt inclusions preserve
349 the initial volatile concentrations due to post-entrapment processes such as CO₂-loss to
350 vapor bubbles (e.g., Wallace et al, 2015) and H-diffusion (Bucholz et al., 2013; Gaetani
351 et al., 2012; Walowski et al., 2015), the dissolved H₂O/CO₂ should nonetheless provide
352 minimum estimates of entrapment depths. For example, Figure 3b shows that the Piton de
353 Caille melt inclusions were trapped at or deeper than ~7.5 km (assuming an average
354 crustal density of 3.0 g/cm³). These minimum depth estimates are within the lower crust
355 (crustal thickness beneath La Réunion is ~12 km; Fontaine et al., 2015) and confirms that
356 the analyzed melt inclusions had far less opportunity for interaction with crustal materials
357 than submarine glasses, decreasing the opportunity of seawater contamination and
358 assimilation of altered oceanic crust (AOC).

359 At La Palma, melt inclusions from each locality sampled more variably degassed
360 melts. Figure 3d shows that all melt inclusion suites, excluding BF02, contain melt
361 inclusions trapped at or greater than ~10.5 km (assuming an average crustal density of 3.0
362 g/cm³). With MOHO depths beneath La Palma estimated at ~12 km (Fullea et al., 2015),
363 these depths of entrapment are within the lower crust, although other mineralogical
364 evidence suggests crystallization of primitive magmas may begin sub-MOHO (Klügel et
365 al., 2005; Nikogosian et al., 2002). This indicates that the least degassed melt inclusions
366 from La Palma had little interaction with crustal materials. It is perhaps not surprising
367 that the least degassed samples from BF01 display the most primitive compositions and
368 are hosted in the highest forsterite olivine measured in this study. Thus, this sample likely

369 provides the most robust estimate of $\delta^{11}\text{B}$ for the HIMU-like mantle source beneath La
370 Palma.

371 In addition to focusing on un-degassed melt inclusions, Figure 4 shows variability
372 of $\delta^{11}\text{B}$ with independent metrics that may indicate assimilation of hydrothermally altered
373 lithologies. For example, if $\delta^{11}\text{B}$ was influenced by assimilation during crustal transit and
374 magmatic evolution, positive correlations would be expected between $\delta^{11}\text{B}$ and B
375 concentrations, while negative correlations would be expected between $\delta^{11}\text{B}$ and host
376 olivine Fo%. Furthermore, assessment of sea-water related contamination can be obtained
377 from ratios of halogens to other incompatible elements, such as Cl/K (Stroncik and
378 Haase, 2004; Kendrick et al., 2014) due to the high abundance of halogens in seawater.
379 Previous work has shown the relationships between Cl/K versus K can be used to
380 discriminate between seawater contamination, degassing and magmatic fractionation
381 (Stroncik and Haase, 2004). For our samples, we find that each suite of melt inclusions
382 shows no meaningful correlations between $\delta^{11}\text{B}$ and B, Cl/K₂O, or the composition
383 (Fo%) of host olivine crystals that might hint at crustal contamination (Fig. 4). Rather,
384 each suite shows variability only with respect to $\delta^{11}\text{B}$ (y-axis; Fig. 4). This pattern
385 indicates that for most samples, the range of $\delta^{11}\text{B}$ within a given melt inclusion suite is
386 related to analytical uncertainty of the $\delta^{11}\text{B}$ measurement, and is not the result of a
387 magmatic process.

388 Conversely, subaerial glasses from BF01 display elevated $\delta^{11}\text{B}$ and B relative to
389 BF01 MI, but have lower values of Cl/K₂O as the result of degassing (Fig. 4a and b).
390 Because Cl is degassed, it is not possible to use halogens to identify assimilation of
391 seawater-altered material for this sample (BF01 glass). However, the statistically

392 significant change in $\delta^{11}\text{B}$ between melt trapped at depth as inclusions and a more
393 evolved melt erupted as glass at the surface suggests that minor contamination may have
394 occurred during magmatic evolution after melt inclusion entrapment. Additionally, melt
395 inclusions from BF02 also contain higher concentrations of B and isotopically heavier
396 $\delta^{11}\text{B}$ compared to BF01 melt inclusions, which are derived from a proximal locality. In
397 addition to melt inclusions being degassed (Fig. 3d, Fig. 4b) and compositionally evolved
398 (Fig. 4c), similar to the BF01 subaerial glass, this observation provides evidence that
399 BF02 may have experienced minor amounts of B contamination, and thus, should not be
400 used to determine mantle source $\delta^{11}\text{B}$. Therefore, we exclude BF02 and BF01 glass from
401 the remainder of the discussion figures and analyses. As discussed above, all other
402 samples from both La Palma and La Réunion show no systematic variation in B, $\delta^{11}\text{B}$,
403 host-olivine Fo, or halogens, which highlights that undegassed melt inclusions retain
404 $\delta^{11}\text{B}$ values most representative of the mantle source region, and are not likely influenced
405 by assimilation en route to the surface.

406

407 **5.2 The $\delta^{11}\text{B}$ composition of the primitive mantle**

408 Due to the ability for boron isotopes to trace recycled materials in the deep
409 mantle, a number of studies have used the boron isotopic system to characterize the OIB
410 reservoirs that have been consistently recognized by Sr-Nd-Pb isotopes (Fig. 5; e.g.,
411 Chaussidon and Jambon, 1994; Chaussidon and Marty, 1995; Chaussidon and Marty
412 1995; Gurenko and Chaussidon 1997; Roy-Barman et al. 1998; Tanaka and Nakamura,
413 2005; Brounce et al., 2012; and Genske et al., 2014). A comprehensive attempt to
414 characterize the $\delta^{11}\text{B}$ composition of the ‘primitive mantle’ as sampled by OIB is

415 described in Chaussidon and Marty (1995). In this study, submarine glasses from Hawaii,
416 St. Helena, Iceland, Macdonald Seamount, Afar, and the Galapagos were analyzed. The
417 results found a large range in $\delta^{11}\text{B}$ (-15 to +7‰), and thus, an “OIB source” $\delta^{11}\text{B}$ had to
418 be calculated based on the most primitive and highest $^3\text{He}/^4\text{He}$ samples, and was
419 determined to be $-10\pm 2\%$ (Fig. 5). Subsequent work, however, produced contradictory
420 results (e.g., Tanaka and Nakamura, 2005), interpreted their results on a MORB baseline
421 that has since been redefined (Marschall et al., 2017), or most often, identified that
422 samples were contaminated by hydrothermally or seawater altered materials en route to
423 the surface (Fig. 5; Brounce et al., 2012; Gurenko et al., 2014). Thus, a robust value for
424 the $\delta^{11}\text{B}$ composition of the ‘primitive mantle’ or OIB-mantle-source has remained
425 elusive.

426 Recent work by Marschall et al. (2017), however, does provide a well-constrained
427 value for pristine, uncontaminated MORB (and the DMM) of $-7.1\pm 0.9\%$. The study,
428 which investigated 56 MORBs from the Mid-Atlantic Ridge, the Southwest Indian Ridge,
429 and the East Pacific Rise and carefully screened for contamination utilizing Cl/K (which
430 was shown to elevate $\delta^{11}\text{B}$ to values as high as $-2.2\pm 1.7\%$), also found no difference
431 between N-MORB and E-MORB reservoirs. Additional $\delta^{11}\text{B}$ for samples from the South
432 Atlantic were presented by Dixon et al. (2017), the compositions of which ($\delta^{11}\text{B}=-$
433 $7.7\pm 1.9\%$) were close to that of the Marschall et al. (2017) MORB datum. The samples
434 were derived from the plume-influenced Discovery and Shona anomalies and are
435 therefore not representative for uncontaminated MORB. However, depleted samples (i.e.,
436 closest to MORB compositions) averaged to lower $\delta^{11}\text{B}$ than enriched samples ($-$
437 $9.2\pm 1.5\%$ vs $-6.4\pm 1.1\%$), suggesting that perhaps the South Atlantic mantle might be

438 lighter than average MORB mantle. Further work will be needed to confirm this as the
439 Dixon et al. (2017) samples were not as rigorously screened for the effects of shallow
440 crustal processes as the Marschall et al. (2017) data, which may have contributed to the
441 variability. This considered, because we use similar standard materials and reference
442 values as Marschall et al., (2017) and described in Marschall and Monteleone (2015), we
443 subsequently compare our results confidently to this MORB datum.

444 Several aspects of La Réunion magmas point to a source little disturbed by recent
445 plate recycling (see section 2.1) and so our multiple, well-clustered $\delta^{11}\text{B}$ analyses from
446 La Réunion should provide a useful estimate for the deep, primitive mantle. Our mean
447 $\delta^{11}\text{B}$ for La Réunion ($-7.9\pm 0.5\%$) overlaps within uncertainty of the global MORB
448 dataset ($-7.1\pm 0.9\%$), suggesting that the primitive mantle may be indistinguishable from
449 MORB with respect to $\delta^{11}\text{B}$. Alternatively, because La Réunion is produced by relatively
450 large degrees of melting relative to other OIB, indicated by tholeiitic compositions and
451 trace element models (see Supplementary Fig. 2), this observation may be explained by
452 boron acquired in the upper mantle. That is, a low-B concentration primitive mantle
453 component may be diluted by MORB-source mantle B and $\delta^{11}\text{B}$ during partial melting or
454 re-equilibration in the uppermost mantle.

455

456 **5.3 Boron in the mantle source**

457 To better constrain the boron isotope systematics at La Palma and La Réunion, it
458 is necessary to understand the relative abundance of boron in the mantle source regions.
459 The major element compositions of melt inclusions from La Palma, which are silica-
460 undersaturated, and La Réunion, which extend to tholeiitic compositions, alone

461 emphasize the petrogenetic differences between these two suites. Therefore, to determine
462 whether or not source variability exists with respect to B, it is useful to consider
463 differences in the degree of partial melting of mantle source regions. Relationships
464 between Zr/Y and La/Y (Supplementary Fig. 2) are used to quantify different degrees of
465 melting and show that La Palma samples represent smaller degree partial melts (2-3%)
466 compared with La Réunion samples (~10%), and affirm that all melts were
467 predominantly generated in the garnet-facies mantle. Using a simple modal batch melting
468 equation, the estimated melt percent, and a range in estimated bulk partition coefficients
469 for B (using the analogs $D_{Pr} = 0.026$ and $D_{Ce} = 0.017$; Marschall et al., 2017), a mantle
470 source B concentration can be calculated for each locality. To achieve the average B
471 concentration measured in La Réunion melt inclusions (2.46 $\mu\text{g/g}$) in a 10% partial melt,
472 the mantle source should contain ~0.31-0.28 $\mu\text{g/g}$ B. For the most primitive sample from
473 La Palma, BF01, an average measured B concentration of 2.36 $\mu\text{g/g}$ is achieved from
474 melting a mantle source with ~0.14-0.11 $\mu\text{g/g}$ by 3%. These results highlight that, despite
475 similar averages in measured melt B concentrations, the mantle source beneath La Palma
476 is estimated to contain less than half as much B as the mantle source beneath La Réunion,
477 although both OIB source regions contain higher concentrations than estimates for the
478 depleted-MORB-mantle (0.077 $\mu\text{g/g}$; Marschall et al., 2017).

479 Due to the inherent uncertainty with melting models, we can additionally explore
480 source heterogeneity through comparison of trace element ratios (e.g., Jochum et al.,
481 1989). During mantle melting, B exhibits similar incompatibility to light REE, such as Ce
482 and La, and partitions similarly to Be, Pr, Pb, and Zr during basalt fractionation
483 (Marschall et al., 2017). Thus, Figure 6 shows the covariance of B/Zr and B/Ce with

484 respect to $\delta^{11}\text{B}$. The distinctly lighter $\delta^{11}\text{B}$ signatures of La Palma samples correlates with
485 lower B/Zr and B/Ce than at La Réunion. This relationship, in conjunction with the
486 calculated mantle source B concentrations, suggests that the mantle source reservoir for
487 the La Palma HIMU-like magmas has lower concentrations of B than the primitive
488 mantle reservoir sampled at La Réunion.

489

490 **5.5 The $\delta^{11}\text{B}$ variability in OIB mantle sources**

491 As discussed in section 2.2, previous work has shown that the mantle source
492 beneath La Palma has clear contributions from a recycled component (e.g., Day et al.,
493 2010). Our new B isotopes results are consistent with these previous hypotheses in that
494 La Palma samples show anomalously low $\delta^{11}\text{B}$, B/Zr, and B/Ce. Thus, the mantle source
495 at La Palma requires a component with isotopically light B and low B abundance. Light
496 boron isotope signatures can be generated at or near the surface and are typically found in
497 material such as continental crust and siliceous oceanic sediments (e.g., Marschall, 2018;
498 Trumbull and Slack, 2018). However, in addition to a light $\delta^{11}\text{B}$ signature, the La Palma
499 mantle source has B concentrations depleted relative to MORB that cannot be simply
500 explained by the mixing of these B-enriched materials (i.e., sediment or continental crust)
501 into the mantle, as this would create a source enriched in B relative to MORB or the
502 primitive mantle. Nor are the radiogenic isotopic signatures consistent with the
503 contribution of continental material. Therefore, a preferred explanation of a B-depleted
504 and isotopically light mantle source is derived from subducted oceanic lithosphere that
505 has been effectively stripped of B during subduction dehydration, consistent with

506 observations at arc volcanoes (e.g., Ryan et al., 1995; Walowski et al., 2016; De Hoog
507 and Savov, 2018 and references there within).

508 To test this hypothesis, we model mixing a 3% partial melt of a hypothetical
509 “dehydrated oceanic lithosphere” endmember with an upper mantle melt (Fig. 7; average
510 MORB defined by Marschall et al., 2017). Due to uncertainty in the fractionation of $\delta^{11}\text{B}$
511 during subduction dehydration, we utilize two different model endmembers to represent
512 the recycled component. The first endmember, with a $\delta^{11}\text{B}$ value of -35‰, is based on the
513 oceanic lithosphere dehydration model of Marschall et al., (2007a), assuming a phengite-
514 free eclogite lithology at 2.5 GPa. However, recent experimental constraints indicate the
515 pH of supercritical fluids during subduction dehydration may be more alkaline than
516 previous suggested (Galvez et al., 2017), and thus, in addition to uncertainty in
517 fractionation factors, the fractionation of $\delta^{11}\text{B}$ fractionation at depth may not be as
518 significant as previously understood. Hence, we additionally model mixing using the $\delta^{11}\text{B}$
519 model results of Konrad-Schmolke and Halama (2014). We find that mixing of a
520 dehydrated slab endmember with $\delta^{11}\text{B}$ values from -11 to -22‰ (correlated to depths of
521 slab dehydration between ~140-200 km depth; Konrad-Schmolke and Halama, 2014)
522 best-predicts the range in measured $\delta^{11}\text{B}$ from the La Palma melt inclusion suites. The
523 mixing model further indicate that the La Palma magmas have ~65-85% of their B
524 contributed from the recycled component, although uncertainty of this simplified model
525 can influence the exact mixing proportions with MORB. Additional uncertainty arises
526 from the fact that the subduction dehydration model endmembers (i.e., Marschall et al.,
527 2007a; Konrad-Schmolke and Halama, 2014) utilize modern seawater compositions ($\delta^{11}\text{B}$
528 = +39.5‰), although the hypothesized recycled component in the La Palma HIMU-

529 source is <1.8 Ga (Day et al., 2010). While the $\delta^{11}\text{B}$ of Precambrian seawater is poorly
530 constrained (Marschall et al., 2018), published estimates for Archean seawater
531 (+14±15‰ and +27±11‰, Grew et al., 2015 and Chaussidon and Appel, 1997,
532 respectively) are isotopically lighter than modern seawater, which would necessitate an
533 even lighter model endmember. Despite these various uncertainties, the mixing model
534 results importantly highlight that dehydrated recycled oceanic lithosphere retains enough
535 B to leverage the $\delta^{11}\text{B}$ composition and produce the B concentrations and isotopic values
536 observed in the La Palma mantle source.

537

538 **5.4 The volatile composition of OIB mantle sources**

539 In addition to understanding how two different deep mantle sources compare in
540 their $\delta^{11}\text{B}$ systematics compared to MORB, a secondary goal of this study is to better
541 understand the concentrations and distribution of volatiles in deep recycled mantle
542 material. To this end, Figure 8a and 8b show the covariance of $\text{H}_2\text{O}_{\text{max}}/\text{Ce}$ ($\text{H}_2\text{O}_{\text{max}}$
543 referring to the maximum H_2O measured in each melt inclusion suite as a best estimate
544 for initial H_2O content) with $\delta^{11}\text{B}$ and $^{206}\text{Pb}/^{204}\text{Pb}$. Consistent with observations of B/Zr
545 and the dehydrated oceanic lithosphere source hypothesis, La Palma samples have a
546 lower $\text{H}_2\text{O}_{\text{max}}/\text{Ce}$ than samples from La Réunion and MORB (Fig. 8a), producing positive
547 correlations between $\text{H}_2\text{O}_{\text{max}}/\text{Ce}$ and $\delta^{11}\text{B}$. During slab dehydration, H_2O is progressively
548 stripped from the slab, while Ce is buffered in the presence of epidote (Carter et al.,
549 2015), producing order of magnitude decreases in $\text{H}_2\text{O}/\text{Ce}$ with increasing T and P (e.g.,
550 Cooper et al., 2012). Therefore, dehydrated oceanic lithosphere would be expected to
551 have low $\text{H}_2\text{O}_{\text{max}}/\text{Ce}$ ratios (i.e., BF01 $\text{H}_2\text{O}_{\text{max}}/\text{Ce} = 187$). It is notable that the observed

552 H_2O_{\max}/Ce is even more depleted than most MORB ($H_2O_{\max}/Ce = 150-400$) and the
553 primitive mantle (La Réunion $H_2O_{\max}/Ce = 252$). Interestingly, this observation is
554 consistent with previous studies on HIMU melts, which also find H_2O_{\max}/Ce values lower
555 than MORB. For example, the HIMU mantle source at Mangaia was determined by
556 Cabral et al. (2014) using re-homogenized melt inclusions to have a H_2O_{\max}/Ce ratio of
557 ~ 200 , while Dixon et al. (2002) calculated a H_2O_{\max}/Ce ratio of ~ 100 for the HIMU
558 source. Both Cabral et al. (2014) and Dixon et al. (2002) conclude that these low primary
559 magmatic H_2O_{\max}/Ce ratios are consistent with significant dehydration of oceanic crust of
560 $>80\%$ efficiency during subduction, followed by long-term storage in the mantle. Similar
561 to the mixing model described in Figure 7, we also model mixing between an upper
562 mantle melt and the two potential HIMU endmembers determined by Dixon et al. (2002)
563 and Cabral et al. (2014; Fig. 8a). Figure 8 shows that the La Palma melts are best
564 explained by mixing of the lower H_2O_{\max}/Ce HIMU source, as determined by Dixon et
565 al., (2002), with either enriched or depleted upper mantle melts. Conversely, the Mangaia
566 HIMU endmember has H_2O_{\max}/Ce values that are too elevated to reproduce the measured
567 values at La Palma. These results provide additional support that the HIMU source
568 reservoir is likely depleted in both H_2O and B due to efficient stripping of these light
569 elements during subduction dehydration.

570 Despite the possibility of CO_2 post-entrapment loss to vapor bubbles for which we
571 have not corrected, undegassed melt inclusions from La Palma retain some of the highest
572 CO_2 contents directly measured in OIB (up to 4303 $\mu g/g$; e.g., Koleszar et al., 2009).
573 These high CO_2 concentrations are similar to previous studies of HIMU melt inclusions
574 (e.g., Cabral et al., 2014) and are consistent with the experimental studies that require a

575 carbonated protolith in the mantle source in order to generate highly alkaline rocks and
576 small degree partial melts (e.g., Kiseeva et al., 2013). That considered, $\text{CO}_{2\text{max}}/\text{Nb}$ ratios
577 of La Palma melt inclusions (~40-60) are lower than those at La Réunion (~70-95), and
578 both significantly lower than MORB (~530; Cartigny et al., 2008).

579

580 **6. Conclusion**

581 Although it has been well-established that recycling of the lithosphere via
582 subduction drives the chemical evolution of the mantle, the character and distribution of
583 volatiles in various mantle reservoirs remains uncertain. In this study, we provide new
584 contributions that improve this understanding through a comparison of the volatile and
585 $\delta^{11}\text{B}$ compositions of olivine-hosted melt inclusions from contrasting OIB endmembers
586 from La Palma, Canary Islands, and La Réunion Island. Our new dataset shows that
587 tephra-derived olivine-hosted melt inclusions are protected from contamination during
588 ascent and provide more robust estimates of primary $\delta^{11}\text{B}$ than previous bulk rock
589 studies, highlighting that the aforementioned OIB reservoirs have distinctly different $\delta^{11}\text{B}$
590 compositions. That is, tholeiitic basalts from La Réunion Island have $\delta^{11}\text{B}$ signatures (-
591 $7.9\pm 0.5\text{‰}$) that overlap with the global MORB dataset ($-7.1\pm 0.9\text{‰}$), while HIMU-like
592 alkali basalts from La Palma, Canary Islands display $\delta^{11}\text{B}$ compositions which extend to
593 lighter values ($-10.5\pm 0.7\text{‰}$). In concert with B/Zr and $\text{H}_2\text{O}/\text{Ce}$, these results provide
594 evidence that the mantle source sampled at La Réunion, representative of a deeply
595 sourced primitive mantle, is indistinguishable from MORB with respect to B and H_2O .
596 Because the La Réunion source has been shown to have little to no influence from
597 recycled components, we hypothesize that either the primitive mantle has an isotopic

598 fingerprint indistinguishable from MORB or that B concentrations are sufficiently low
599 that they are diluted by partial melting that occurs in the uppermost mantle. Conversely,
600 we find the HIMU-like mantle source beneath La Palma contains low-B and low-H₂O,
601 which is best explained by contributions from a recycled oceanic lithosphere component
602 significantly dehydrated and isotopically fractionated within the ‘subduction factory,’ in
603 the uppermost mantle. Our results provide new support for the role of complex and step-
604 wise subduction zone processing in the generation of radiogenic Pb-isotopic signatures,
605 and the decoupling volatiles and light stable isotopes from other lithophile elements in
606 OIB mantle reservoirs.

607

608 **Acknowledgements**

609 We thank J. Craven and R. Hinton for assistance with the SIMS measurements, C.
610 Hayward for assistance with the EPMA, and B. Upton for providing the Piton de Caille
611 samples. We also thank H. Marschall and J. Ryan for their insightful reviews and M.
612 Bickle for editorial handling. Constructive discussions facilitated by NERC Deep
613 Volatiles Consortium meetings are gratefully acknowledged. Funding was provided by
614 National Environmental Research Council grant NE/M000443/1.

615

616 **Table Captions**

617 *Table 1: Average melt inclusion compositions. Average compositions refer to the average*
618 *MI composition calculated from the full suite of analyzed melt inclusions (n = X refers to*
619 *number of melt inclusions from each sample). Major element uncertainty calculated as*
620 *one standard deviation of the population used to calculate the average from MI suite*

621 (including analytical uncertainty). The complete corrected and uncorrected dataset of
622 individual MI compositions can be found in Supplementary Tables TS2 and TS3.
623 ^aInitial Fe contents used in the calculations were chosen based either on the FeO^T of the
624 bulk tephra or the highest value of FeO^T for MI from a particular cone.
625 ^bH₂O_{max} values represent the highest from each cone after post-entrapment crystallization
626 correction
627 ^cCO_{2max} values represent the highest from each cone after post-entrapment crystallization
628 correction
629 ^dRefers to the average percent olivine addition required to reach equilibrium with host
630 olivine compositions

631

632 **Figure Captions**

633 *Figure 1: Sample Localities.* (a) Topographic shade map showing the relative location of
634 sampled ocean islands; the Canary Island Archipelago is off the northwestern coast of the
635 African continent and the island of La Réunion is off the eastern coast of Madagascar. (b)
636 Topographic shade map depicting the island of La Réunion and highlighting the location
637 of the Piton de Caille, the cinder cone sampled for this study. (c) Regional map of the
638 Canary Island chain showing the location of La Palma relative to the other islands of the
639 archipelago. La Palma and El Hierro represent the youngest islands in a generally
640 westward-younging chain. (d) Topographic shade map of La Palma showing individual
641 sample localities, Barranco de Fagundo, a Holocene Cone, and Vólcan Duraznero, which
642 erupted in 1949. Basemaps generated with GeoMapApp (<http://www.geomapapp.org>;
643 Ryan et al., 2009).

644

645 *Figure 2:* The $^{87}\text{Sr}/^{86}\text{Sr}$ and $^{206}\text{Pb}/^{204}\text{Pb}$ of OIB globally. Individual colored data points as
646 described in the legend represent previously published bulk rock values from the sample
647 localities used in this study (B. Fagundo, Holocene Cone, and Vólcan Duraznero, from
648 Day et al., 2010; and La Réunion: Albaréde et al., 1997 and references there within). The
649 larger maroon shaded region outlines previously published data from La Réunion Island
650 and Piton de la Fournaise volcano (Albaréde et al., 1997 and references there within) and
651 the teal shaded region represents all previously published data from other samples from
652 the Cumbre Vieja Rift Zone and the Taburiente Shield at La Palma (Praegel et al., 2006;
653 Day et al., 2010). The grey shaded regions represent previously published datasets from
654 notable ocean island endmembers (data from the GEOROC Database [http://georoc.mpch-](http://georoc.mpch-mainz.gwdg.de/georoc/)
655 [mainz.gwdg.de/georoc/](http://georoc.mpch-mainz.gwdg.de/georoc/) and references there within). Colors and symbols for La Palma
656 and Réunion samples as described in the legend are consistent throughout the following
657 figures.

658

659 *Figure 3:* Melt inclusion major element and volatile compositions compared to
660 previously published melt inclusion and bulk rock data. All melt inclusions from La
661 Palma and La Réunion plotted in this figure are corrected for post-entrapment
662 crystallization as described in Section 5.3 (Supplementary Table TS2 and TS3). (a,c)
663 MgO versus Al_2O_3 contents of melt inclusions from (a) Piton Caille compared to
664 previously published data from La Réunion Island, including melt inclusion data from
665 Piton Caille (Bureau et al., 1998), proximal Holocene cinder cones (Dolomieu and Piton
666 Vincenzo; Bureau et al., 1998), and Piton de la Fournaise (Vigouroux et al., 2009), and

667 whole rock data from Piton de La Fournaise (Albarède et al., 1997). (c) La Palma melt
668 inclusion data compared to previously published whole rock data from both the Cumbre
669 Vieja Rift and Taburiente Shield (Day et al., 2010). The overlapping red bars indicate an
670 approximation for the most primitive compositions from each island, and red arrows
671 show the influence of olivine and pyroxene fractionation of accumulation from that
672 parental melt composition. (b, d) H₂O versus CO₂ contents of (b) La Réunion and (d) La
673 Palma melt inclusions with vapor saturation isobars generated using Sol_Ex (grey lines;
674 Witham et al., 2012) and open-system degassing paths (black lines) from Newman and
675 Lowenstern (2002). The Sol_Ex input composition (open star symbol) is based on major
676 element data the most primitive and un-degassed melt inclusion from each individual
677 sample. We interpret nearly vertical trends in H₂O versus CO₂ as CO₂ degassing prior to
678 entrapment, while variability in H₂O away from open system degassing paths is likely the
679 result of post-entrapment diffusive H₂O-loss.

680

681 *Figure 4:* The $\delta^{11}\text{B}$ composition of individual melt inclusions versus (a) B ($\mu\text{g/g}$), (b)
682 Cl/K₂O, and (c) the forsterite percent of host olivine crystals. The B, Cl, and K₂O
683 concentrations from all MI plotted in this figure are corrected for post-entrapment
684 crystallization as described in Section 5.3 (Supplementary Table TS2 and TS3). Each
685 panel is used as a different method to test whether $\delta^{11}\text{B}$ is changing as a function of
686 magmatic evolution driven by assimilation of B-enriched material (i.e., seawater or
687 seawater altered materials) or fractional crystallization. Each sample suite of melt
688 inclusions show no meaningful positive or negative correlations between $\delta^{11}\text{B}$ and (a) B
689 ($\mu\text{g/g}$), (b) Cl/K₂O, or (c) the forsterite percent of host olivine crystals. Rather, each suite

690 shows variability only with respect to $\delta^{11}\text{B}$ (y-axis). This pattern indicates that for most
691 samples, the range of $\delta^{11}\text{B}$ represents the analytical uncertainty, and is not the result of a
692 magmatic process. That being said, B. Fagundo 02 has heavier $\delta^{11}\text{B}$ values with elevated
693 B ($\mu\text{g/g}$) concentrations and hosts MI in lower forsterite olivine crystals when compared
694 to melt inclusions from a similar location, B. Fagundo 01. Although these samples are
695 different, their proximal location and geochemical relationship suggests that B. Fagundo
696 02 melt inclusions may have altered $\delta^{11}\text{B}$ values and do not provide robust estimates of
697 the mantle source $\delta^{11}\text{B}$, as indicated by the red arrow labeled “assimilation”. Thus, B.
698 Fagundo 01, are utilized exclusively in the following figures as the most robust estimate
699 of primary $\delta^{11}\text{B}$ for the B. Fagundo locality at La Palma.

700

701 *Figure 5:* The average $\delta^{11}\text{B}$ composition of samples from this study compared to a
702 selection of previously published OIB samples. The filled colored symbols represent the
703 average $\delta^{11}\text{B}$ of each melt inclusion suite (# of inclusions for each sample as in *Table 1*)
704 from La Palma and La Réunion, with error bars/symbol size representing 2σ uncertainty.
705 The grey bar represents MORB with 2σ uncertainty (Marschall et al., 2017). Black
706 symbols represent individual analyses of submarine glassed from Hawaii, the Galapagos,
707 the Azores, and St. Helena (Chaussidon and Marty, 1995). The black rectangle labeled
708 “OIB” is a calculated “OIB source” composition as described in Chaussidon and Marty
709 (1995), with a 2σ uncertainty. Grey diamonds represent analyses of individual melt
710 inclusions from Lakagígar, Iceland, with the largest symbol representing the best estimate
711 of the initial $\delta^{11}\text{B}$ (Brounce et al., 2012). Grey triangles represent analyses of individual
712 melt inclusions from the Azores (Flores and Corvo), with the largest symbol representing

713 the best estimate of the initial $\delta^{11}\text{B}$ (Genske et al., 2014). Grey crosses represent lavas
714 from Hawaii (Koolau, Kilauea, and Mauna Loa; Tanaka and Nakamura, 2005). For a
715 detailed overview of all currently published OIB B-isotope data, see Marschall, 2018.

716

717 *Figure 6: $\delta^{11}\text{B}$ versus B/Zr for MI suite averages with error bars that represent*
718 *2σ uncertainty, and the individual MI compositions from which the averages are*
719 *calculated. The B and Zr concentrations from all MI data plotted in this figure are*
720 *corrected for post-entrapment crystallization as described in Section 5.3 (Supplementary*
721 *Table TS2 and TS3). Because B has is similarly incompatible to Zr (Marschall et al.,*
722 *2017), ratios of these elements can be used to assess relative mantle source B*
723 *abundances, despite difference in degree of mantle melting or minor amounts of crystal*
724 *fractionation. The black diamond represents the average MORB composition as defined*
725 *by Marschall et al. (2017).*

726

727 *Figure 7: $\delta^{11}\text{B}$ versus B/Zr for MI suite averages with error bars that represent*
728 *2σ uncertainty, data as described in Fig. 6. Plotted curves represent mixing between a 3%*
729 *partial melt of a hypothetical recycled mantle component (black and grey hexagons;*
730 *dehydrated oceanic lithosphere) with average MORB (Marschall et al., 2017; black oval).*
731 *The $\delta^{11}\text{B}$ value for the isotopically light recycled endmember (grey hexagon) is based on*
732 *the model results of Marschall et al. (2007a), while the $\delta^{11}\text{B}$ for the heavier recycled*
733 *component (black hexagon) is based on the range in model results from Konrad-*
734 *Schmolke and Halama (2014; black hexagon) that best-predict the measured $\delta^{11}\text{B}$*

735 compositions. The Zr composition is derived from a refractory eclogite composition
736 (Rudnick et al., 2002 and references there within).
737
738 *Figure 8: H₂O_{max}/Ce versus (a) δ¹¹B versus and (b) ²⁰⁶Pb/²⁰⁴Pb. Colored symbols for MI*
739 *suite averages from this study as described in legend with 2σ error bars. Plotted curves on*
740 *panel (a) represent mixing between a 3% partial melt of previously determined HIMU*
741 *mantle reservoirs (black stars; Mangaia HIMU from Cabral et al., 2014; ‘HIMU source’*
742 *from Dixon et al., 2002) with both S. Mid-Atlantic Ridge MORB (grey hexagon) and*
743 *Arctic Ridge MORB (black hexagon; Dixon et al., 2017). Panel (b) shows a comparison*
744 *of previously published submarine MORB glass data (Dixon et al., 2017) and OIB data*
745 *(Tanaka et al., 2002, Hémond et al., 1994, Workman et al., 2004, Snyder et al., 2004 and*
746 *references there within). The δ¹¹B is based on the range in model results (-17 to -11‰;*
747 *from Konrad-Schmolke and Halama, 2014) that best-predict the measured δ¹¹B*
748 *compositions.*

749

750 **References**

- 751 Allègre, C. J. (1982). Chemical geodynamics. *Tectonophysics*, 81(3-4), 109-132.
- 752
- 753 Albarède, F., Luais, B., Fitton, G., Semet, M., Kaminski, E., Upton, B. G. J., & Cheminée,
754 J. L. (1997). The geochemical regimes of Piton de la Fournaise volcano (Réunion) during
755 the last 530,000 years. *Journal of Petrology*, 38(2), 171-201.
- 756

757 Borisov, A. A., & Shapkin, A. I. (1990). A new empirical equation rating Fe³⁺/Fe²⁺ in
758 magmas to their composition, oxygen fugacity, and temperature. *Geochem. Int*, 27(1),
759 111-116.

760

761 Brounce, M., Feineman, M., LaFemina, P., & Gurenko, A. (2012). Insights into crustal
762 assimilation by Icelandic basalts from boron isotopes in melt inclusions from the 1783–
763 1784 Lakagigar eruption. *Geochimica et Cosmochimica Acta*, 94, 164-180.

764

765 Brounce M., Stolper E., Peterson M., & Eiler J. (2017). Goldschmidt Abstracts, 2017,
766 475.

767

768 Bucholz, C. E., Gaetani, G. A., Behn, M. D., & Shimizu, N. (2013). Post-entrapment
769 modification of volatiles and oxygen fugacity in olivine-hosted melt inclusions. *Earth
770 and Planetary Science Letters*, 374, 145-155.

771

772 Bureau, H., Pineau, F., Métrich, N., Semet, M. P., & Javoy, M. (1998). A melt and fluid
773 inclusion study of the gas phase at Piton de la Fournaise volcano (Réunion
774 Island). *Chemical geology*, 147(1-2), 115-130.

775

776

777 Cabral, R. A., Jackson, M. G., Koga, K. T., Rose-Koga, E. F., Hauri, E. H., Whitehouse,
778 M. J., ... & Kelley, K. A. (2014). Volatile cycling of H₂O, CO₂, F, and Cl in the HIMU

779 mantle: A new window provided by melt inclusions from oceanic hot spot lavas at
780 Mangaia, Cook Islands. *Geochemistry, Geophysics, Geosystems*, 15(11), 4445-4467.
781

782 Carter, L. B., Skora, S., Blundy, J. D., De Hoog, J. C. M., & Elliott, T. (2015). An
783 experimental study of trace element fluxes from subducted oceanic crust. *Journal of*
784 *Petrology*, 56(8), 1585-1606.
785

786 Cartigny, P., Pineau, F., Aubaud, C., & Javoy, M. (2008). Towards a consistent mantle
787 carbon flux estimate: Insights from volatile systematics (H₂O/Ce, δD, CO₂/Nb) in the
788 North Atlantic mantle (14 N and 34 N). *Earth and Planetary Science Letters*, 265(3-4),
789 672-685.
790

791 Chase, C. G. (1981). Oceanic island Pb: two-stage histories and mantle evolution. *Earth*
792 *and Planetary Science Letters*, 52(2), 277-284.
793

794 Chaussidon, M., & Jambon, A. (1994). Boron content and isotopic composition of
795 oceanic basalts: geochemical and cosmochemical implications. *Earth and Planetary*
796 *Science Letters*, 121(3-4), 277-291.
797

798 Chaussidon, M., & Marty, B. (1995). Primitive boron isotope composition of the
799 mantle. *Science*, 269(5222), 383-386.
800

801 Chaussidon, M., & Appel, P. W. U. (1997). Boron isotopic composition of tourmalines
802 from the 3.8-Ga-old Isua supracrustals, West Greenland: implications on the $\delta^{11}\text{B}$ value
803 of early Archean seawater. *Chemical Geology*, 136(3-4), 171-180.

804

805 Chauvel, C., Hofmann, A. W., & Vidal, P. (1992). HIMU-EM: the French Polynesian
806 connection. *Earth and Planetary Science Letters*, 110(1-4), 99-119.

807

808 Cooper, L. B., Ruscitto, D. M., Plank, T., Wallace, P. J., Syracuse, E. M., & Manning, C.
809 E. (2012). Global variations in H₂O/Ce: 1. Slab surface temperatures beneath volcanic
810 arcs. *Geochemistry, Geophysics, Geosystems*, 13(3).

811

812 Danyushevsky, L. V., Della-Pasqua, F. N., & Sokolov, S. (2000). Re-equilibration of
813 melt inclusions trapped by magnesian olivine phenocrysts from subduction-related
814 magmas: petrological implications. *Contributions to Mineralogy and Petrology*, 138(1),
815 68-83.

816

817 Danyushevsky, L. V., & Plechov, P. (2011). Petrolog3: Integrated software for modeling
818 crystallization processes. *Geochemistry, Geophysics, Geosystems*, 12(7).

819

820 Day, J. M., Pearson, D. G., Macpherson, C. G., Lowry, D., & Carracedo, J. C. (2010).
821 Evidence for distinct proportions of subducted oceanic crust and lithosphere in HIMU-
822 type mantle beneath El Hierro and La Palma, Canary Islands. *Geochimica et*
823 *Cosmochimica Acta*, 74(22), 6565-6589.

824

825 De Hoog, C. J., & Savov, I. P. (2017). Subduction zones, dehydration, metasomatism,
826 mud and serpentinite volcanoes, and arc magmatism. *Boron isotopes—The fifth element,*
827 *advances in isotope geochemistry*, 7, 219-249.

828

829 Dixon, J. E., Leist, L., Langmuir, C., & Schilling, J. G. (2002). Recycled dehydrated
830 lithosphere observed in plume-influenced mid-ocean-ridge basalt. *Nature*, 420(6914),
831 385.

832

833 Dixon, J. E., Bindeman, I. N., Kingsley, R. H., Simons, K. K., Le Roux, P. J., Hajewski,
834 T. R., Walowski, K.J., Wada, I. & Wallace, P.J. (2017). Light Stable Isotopic
835 Compositions of Enriched Mantle Sources: Resolving the Dehydration
836 Paradox. *Geochemistry, Geophysics, Geosystems*, 18(11), 3801-3839.

837

838 Eiler, J. M., Farley, K. A., Valley, J. W., Hauri, E., Craig, H., Hart, S. R., & Stolper, E.
839 M. (1997). Oxygen isotope variations in ocean island basalt phenocrysts. *Geochimica et*
840 *Cosmochimica Acta*, 61(11), 2281-2293.

841

842 Esposito, R., Steele-Macinnis, M. J., Fedele, L., & Bodnar, R. J. (2010, June). Evolution
843 of H₂O and CO₂ contents in silicate melt inclusions during post-entrapment
844 crystallization. *Geochimica et Cosmochimica Acta*, 74(12), A272-A272.

845

846 Fontaine, F. R., Barruol, G., Tkalčić, H., Wölbern, I., Rumpker, G., Bodin, T., &
847 Haugmard, M. (2015). Crustal and uppermost mantle structure variation beneath La
848 Réunion hotspot track. *Geophysical Journal International*, 203(1), 107-126.
849

850 Foster, G. L., Pogge von Strandmann, P. A., & Rae, J. W. B. (2010). Boron and
851 magnesium isotopic composition of seawater. *Geochemistry, Geophysics, Geosystems*,
852 11(8).
853

854 Fulla, J., Camacho, A. G., Negredo, A. M., & Fernández, J. (2015). The Canary Islands
855 hot spot: new insights from 3D coupled geophysical–petrological modelling of the
856 lithosphere and uppermost mantle. *Earth and Planetary Science Letters*, 409, 71-88.
857

858 Gaetani, G. A., O’Leary, J. A., Shimizu, N., Bucholz, C. E., & Newville, M. (2012).
859 Rapid reequilibration of H₂O and oxygen fugacity in olivine-hosted melt
860 inclusions. *Geology*, 40(10), 915-918.
861

862 Galvez, M. E., Connolly, J. A., & Manning, C. E. (2016). Implications for metal and
863 volatile cycles from the pH of subduction zone fluids. *Nature*, 539(7629), 420.
864

865 Genske, F. S., Turner, S. P., Beier, C., Chu, M. F., Tonarini, S., Pearson, N. J., & Haase,
866 K. M. (2014). Lithium and boron isotope systematics in lavas from the Azores islands
867 reveal crustal assimilation. *Chemical Geology*, 373, 27-36.
868

869 Grew, E. S., Dymek, R. F., De Hoog, J. C., Harley, S. L., Boak, J., Hazen, R. M., &
870 Yates, M. G. (2015). Boron isotopes in tourmaline from the ca. 3.7–3.8 Ga Isua
871 supracrustal belt, Greenland: Sources for boron in Eoarchean continental crust and
872 seawater. *Geochimica et Cosmochimica Acta*, 163, 156-177.

873

874 Gurenko, A. A., & Chaussidon, M. (1997). Boron concentrations and isotopic
875 composition of the Icelandic mantle: evidence from glass inclusions in olivine. *Chemical*
876 *Geology*, 135(1), 21-34.

877

878 Gurenko, A. A., & Kamenetsky, V. S. (2011). Boron isotopic composition of olivine-
879 hosted melt inclusions from Gorgona komatiites, Colombia: New evidence supporting
880 wet komatiite origin. *Earth and Planetary Science Letters*, 312(1-2), 201-212.

881

882 Harvey, J., Garrido, C. J., Savov, I., Agostini, S., Padrón-Navarta, J. A., Marchesi, C., &
883 Gómez-Pugnaire, M. T. (2014). ¹¹B-rich fluids in subduction zones: The role of antigorite
884 dehydration in subducting slabs and boron isotope heterogeneity in the mantle. *Chemical*
885 *Geology*, 376, 20-30.

886

887 Harvey, J., Savov, I. P., Agostini, S., Cliff, R., Walshaw, R., 2014, Si-metasomatism in
888 serpentized peridotite: the effects of talc-alteration on strontium and boron isotopes in
889 abyssal peridotites from ODP Leg 209, Hole 1268a. *Geochim. Cosmochim. Acta*, 126, 30-
890 48.

891

892 Hémond, C., Devey, C. W., & Chauvel, C. (1994). Source compositions and melting
893 processes in the Society and Austral plumes (South Pacific Ocean): Element and isotope
894 (Sr, Nd, Pb, Th) geochemistry. *Chemical Geology*, 115(1-2), 7-45.
895

896 Hernández-Pacheco, E., & Valls, M. C. (1982). *The historic eruptions of La Palma island*
897 *(Canaries)*.
898

899 Hofmann, A. W., & White, W. M. (1982). Mantle plumes from ancient oceanic
900 crust. *Earth and Planetary Science Letters*, 57(2), 421-436.
901

902 Ishikawa, T., & Nakamura, E. (1993). Boron isotope systematics of marine
903 sediments. *Earth and Planetary Science Letters*, 117(3-4), 567-580.
904

905 Ishikawa, T., & Tera, F. (1999). Two isotopically distinct fluid components involved in
906 the Mariana arc: Evidence from Nb/B ratios and B, Sr, Nd, and Pb isotope
907 systematics. *Geology*, 27(1), 83-86.
908

909 Ishikawa, T., Tera, F., & Nakazawa, T. (2001). Boron isotope and trace element
910 systematics of the three volcanic zones in the Kamchatka arc. *Geochimica et*
911 *Cosmochimica Acta*, 65(24), 4523-4537
912

913 Johnson, E. R., Wallace, P. J., Delgado Granados, H., Manea, V. C., Kent, A. J.,
914 Bindeman, I. N., & Donegan, C. S. (2009). Subduction-related volatile recycling and

915 magma generation beneath Central Mexico: insights from melt inclusions, oxygen
916 isotopes and geodynamic models. *Journal of Petrology*, 50(9), 1729-1764.
917

918 Jung, H., & Karato, S. I. (2001). Water-induced fabric transitions in olivine.
919 *Science*, 293(5534), 1460-1463.
920

921 Kendrick, M. A., Kamenetsky, V. S., Phillips, D., & Honda, M. (2012). Halogen
922 systematics (Cl, Br, I) in mid-ocean ridge basalts: a Macquarie Island case
923 study. *Geochimica et Cosmochimica Acta*, 81, 82-93.
924

925 Kendrick, M. A., Jackson, M. G., Kent, A. J., Hauri, E. H., Wallace, P. J., & Woodhead,
926 J. (2014). Contrasting behaviours of CO₂, S, H₂O and halogens (F, Cl, Br, and I) in
927 enriched-mantle melts from Pitcairn and Society seamounts. *Chemical Geology*, 370, 69-
928 81.
929

930 Kiseeva, E. S., Litasov, K. D., Yaxley, G. M., Ohtani, E., & Kamenetsky, V. S. (2013).
931 Melting and phase relations of carbonated eclogite at 9–21 GPa and the petrogenesis of
932 alkali-rich melts in the deep mantle. *Journal of Petrology*, 54(8), 1555-1583.
933

934 Koleszar, A. M., Saal, A. E., Hauri, E. H., Nagle, A. N., Liang, Y., & Kurz, M. D.
935 (2009). The volatile contents of the Galapagos plume; evidence for H₂O and F open
936 system behavior in melt inclusions. *Earth and Planetary Science Letters*, 287(3), 442-
937 452.

938

939 Kowalski, P., & Wunder, B. (2017). Boron-isotope fractionation among solids-fluids-
940 melts: experiments and atomic modeling. *Boron isotopes—The fifth element, advances in*
941 *isotope geochemistry*, 7, 33-69.

942

943 Klügel, A., Hansteen, T. H., & Galipp, K. (2005). Magma storage and underplating
944 beneath Cumbre Vieja volcano, la Palma (Canary Islands). *Earth and Planetary Science*
945 *Letters*, 236(1), 211-226.

946

947 Konrad-Schmolke, M., & Halama, R. (2014). Combined thermodynamic–geochemical
948 modeling in metamorphic geology: boron as tracer of fluid–rock interaction. *Lithos*, 208,
949 393-414.

950

951 Leeman, W. P., Tonarini, S., Chan, L. H., & Borg, L. E. (2004). Boron and lithium
952 isotopic variations in a hot subduction zone—the southern Washington
953 Cascades. *Chemical Geology*, 212(1), 101-124.

954

955 Lloyd, A. S., Plank, T., Ruprecht, P., Hauri, E. H., & Rose, W. (2013). Volatile loss from
956 melt inclusions in pyroclasts of differing sizes. *Contributions to Mineralogy and*
957 *Petrology*, 165(1), 129-153.

958

959 Marcantonio, F., Zindler, A., Elliott, T., & Staudigel, H. (1996). Os isotope systematics
960 of La Palma, Canary Islands: evidence for recycled crust in the mantle source of HIMU
961 ocean islands. *Oceanographic Literature Review*, 2(43), 153.

962

963 Marschall, H. R., & Monteleone, B. D. (2015). Boron isotope analysis of silicate glass
964 with very low boron concentrations by secondary ion mass spectrometry. *Geostandards
965 and Geoanalytical Research*, 39(1), 31-46.

966

967 Marschall, H. R., Wanless, V. D., Shimizu, N., von Strandmann, P. A. P., Elliott, T., &
968 Monteleone, B. D. (2017). The boron and lithium isotopic composition of mid-ocean
969 ridge basalts and the mantle. *Geochimica et Cosmochimica Acta*, 207, 102-138.

970

971 Marschall, H. R. (2018) Boron isotopes in the ocean floor realm and the mantle. In:
972 Marschall, H. R. & Foster, G. L. (eds.) *Boron Isotopes – The Fifth Element*, vol. 6 of
973 *Advances in Isotope Geochemistry*, chap. 8, 189–215, Springer, Heidelberg

974

975 McBirney, A. R., & Gass, I. G. (1967). Relations of oceanic volcanic rocks to mid-
976 oceanic rises and heat flow. *Earth and Planetary Science Letters*, 2(4), 265-276.

977

978 Michael, P. (1995). Regionally distinctive sources of depleted MORB: Evidence from
979 trace elements and H₂O. *Earth and Planetary Science Letters*, 131(3-4), 301-320.

980

981 Nielsen, S. G., Rehkämper, M., Norman, M. D., Halliday, A. N., & Harrison, D. (2006).
982 Thallium isotopic evidence for ferromanganese sediments in the mantle source of
983 Hawaiian basalts. *Nature*, 439(7074), 314.
984
985 Moore, L. R., Gazel, E., Tuohy, R., Lloyd, A. S., Esposito, R., Steele-MacInnis, M., &
986 Bodnar, R. J. (2015). Bubbles matter: An assessment of the contribution of vapor bubbles
987 to melt inclusion volatile budgets. *American Mineralogist*, 100(4), 806-823.
988
989 Nakamura, E., Ishikawa, T., Birck, J. L., & Allègre, C. J. (1992). Precise boron isotopic
990 analysis of natural rock samples using a boron-mannitol complex. *Chemical*
991 *Geology*, 94(3), 193-204.
992
993 Newman, S., & Lowenstern, J. B. (2002). VolatileCalc: a silicate melt–H₂O–CO₂
994 solution model written in Visual Basic for excel. *Computers & Geosciences*, 28(5), 597-
995 604.
996
997 Nikogosian, I. K., Elliott, T., & Touret, J. L. (2002). Melt evolution beneath thick
998 lithosphere: a magmatic inclusion study of La Palma, Canary Islands. *Chemical*
999 *Geology*, 183(1), 169-193.
1000
1001 Pabst, S., Zack, T., Savov, I. P., Ludwig, T., Rost, D., Tonarini, S., & Vicenzi, E. P.
1002 (2012). The fate of subducted oceanic slabs in the shallow mantle: insights from boron

1003 isotopes and light element composition of metasomatized blueschists from the Mariana
1004 forearc. *Lithos*, 132, 162-179.

1005

1006 Peters, B. J., Carlson, R. W., Day, J. M., & Horan, M. F. (2018). Hadean silicate
1007 differentiation preserved by anomalous $^{142}\text{Nd}/^{144}\text{Nd}$ ratios in the Réunion hotspot
1008 source. *Nature*, 555(7694), 89.

1009

1010 Praegel, N.O., Holm, P.M., (2006). Lithospheric contributions to the high-MgO basanites
1011 from the Cumbre Vieja Volcano, La Palma, Canary Islands and evidence for temporal
1012 variation in plume influence. *Journal of Volcanology and Geothermal Research*,
1013 149(2006), 213-239.

1014

1015 Putirka, K. D. (2005). Mantle potential temperatures at Hawaii, Iceland, and the mid-
1016 ocean ridge system, as inferred from olivine phenocrysts: Evidence for thermally driven
1017 mantle plumes. *Geochemistry, Geophysics, Geosystems*, 6(5).

1018

1019 Rosner, M., Rhede, D., & Erzinger, J. (2004). Heavy boron isotope compositions of back-
1020 arc lavas from the southern Lau-basin (Valu Fa Ridge). *Geochimica et Cosmochimica*
1021 *Acta*, 68, (11A599-A599).

1022

1023 Rosner, M., Wiedenbeck, M., & Ludwig, T. (2008). Composition-induced variations in
1024 SIMS instrumental mass fractionation during boron isotope ratio measurements of silicate
1025 glasses. *Geostandards and Geoanalytical Research*, 32(1), 27-38.

1026

1027 Rosner, M., & Meixner, A. (2004). Boron isotopic composition and concentration of ten
1028 geological reference materials. *Geostandards and Geoanalytical Research*, 28(3), 431-
1029 441.

1030

1031 Ryan, J. G., & Langmuir, C. H. (1993). The systematics of boron abundances in young
1032 volcanic rocks. *Geochimica et Cosmochimica Acta*, 57(7), 1489-1498.

1033

1034 Ryan, J. G., Leeman, W. P., Morris, J. D., & Langmuir, C. H. (1996). The boron
1035 systematics of intraplate lavas: Implications for crust and mantle evolution. *Geochimica
1036 et Cosmochimica Acta*, 60(3), 415-422.

1037

1038 Ryan, J. G., & Kyle, P. R. (2004). Lithium abundance and lithium isotope variations in
1039 mantle sources: insights from intraplate volcanic rocks from Ross Island and Marie Byrd
1040 Land (Antarctica) and other oceanic islands. *Chemical Geology*, 212(1), 125-142.

1041

1042 Ryan, W.B.F., S.M. Carbotte, J.O. Coplan, S. O'Hara, A. Melkonian, R. Arko, R.A.
1043 Weissel, V. Ferrini, A. Goodwillie, F. Nitsche, J. Bonczkowski, and R. Zemsky (2009),
1044 Global Multi-Resolution Topography synthesis, *Geochem. Geophys. Geosyst.*, 10,
1045 Q03014, doi:10.1029/2008GC002332.

1046

1047 Roy-Barman, M., Wasserburg, G. J., Papanastassiou, D. A., & Chaussidon, M. (1998).
1048 Osmium isotopic compositions and Re–Os concentrations in sulfide globules from
1049 basaltic glasses. *Earth and Planetary Science Letters*, 154(1), 331-347.
1050

1051 Savov, I. P., Leeman, W. P., Lee, C. T. A., & Shirey, S. B. (2009). Boron isotopic
1052 variations in NW USA rhyolites: Yellowstone, Snake River Plain, Eastern
1053 Oregon. *Journal of Volcanology and Geothermal Research*, 188(1), 162-172.
1054

1055 Schiano, P., David, K., Vlastélic, I., Gannoun, A., Klein, M., Nauret, F., & Bonnard, P.
1056 (2012). Osmium isotope systematics of historical lavas from Piton de la Fournaise
1057 (Réunion Island, Indian Ocean). *Contributions to Mineralogy and Petrology*, 164(5),
1058 805-820.
1059

1060 Schmincke, H. U. (1982). Volcanic and chemical evolution of the Canary Islands.
1061 In *Geology of the Northwest African continental margin* (pp. 273-306). Springer, Berlin,
1062 Heidelberg.
1063

1064 Smith, H. J., Spivack, A. J., Staudigel, H., & Hart, S. R. (1995). The boron isotopic
1065 composition of altered oceanic crust. *Chemical Geology*, 126(2), 119-135.
1066

1067 Snyder, D. C., Widom, E., Pietruszka, A. J., & Carlson, R. W. (2004). The role of open-
1068 system processes in the development of silicic magma chambers: a chemical and isotopic

1069 investigation of the Fogo A trachyte deposit, São Miguel, Azores. *Journal of*
1070 *Petrology*, 45(4), 723-738.

1071

1072 Sobolev, A. V., & Nikogosian, I. K. (1994). Petrology of long-lived mantle plume
1073 magmatism: Hawaii, Pacific and Reunion Island, *Indian Ocean. Petrology*, 2(2), 111-
1074 144.

1075

1076 Spivack, A. J., & Edmond, J. M. (1987). Boron isotope exchange between seawater and
1077 the oceanic crust. *Geochimica et Cosmochimica Acta*, 51(5), 1033-1043.

1078

1079 Stroncik, N. A., & Haase, K. M. (2004). Chlorine in oceanic intraplate basalts:
1080 Constraints on mantle sources and recycling processes. *Geology*, 32(11), 945-948.

1081 Tanaka, R., & Nakamura, E. (2005). Boron isotopic constraints on the source of
1082 Hawaiian shield lavas. *Geochimica et Cosmochimica Acta*, 69(13), 3385-3399.

1083

1084 Tanaka, R., Nakamura, E., & Takahashi, E. (2002). Geochemical evolution of Koolau
1085 volcano, Hawaii. *Hawaiian Volcanoes: Deep Underwater Perspectives*, 311-332.

1086

1087 Teng, F. Z., Li, W. Y., Ke, S., Marty, B., Dauphas, N., Huang, S., ... & Pourmand, A.
1088 (2010). Magnesium isotopic composition of the Earth and chondrites. *Geochimica et*
1089 *Cosmochimica Acta*, 74(14), 4150-4166.

1090

1091 Tonarini, S., Leeman, W. P., & Leat, P. T. (2011). Subduction erosion of forearc mantle
1092 wedge implicated in the genesis of the South Sandwich Island (SSI) arc: evidence from
1093 boron isotope systematics. *Earth and Planetary Science Letters*, 301(1), 275-284.
1094

1095 Trumbull, R. B., & Slack, J. F. (2018). Boron isotopes in the continental crust: granites,
1096 pegmatites, felsic volcanic rocks, and related ore deposits. In *Boron Isotopes* (pp. 249-
1097 272). Springer, Cham.
1098

1099 Turner, S., Hawkesworth, C., Rogers, N., & King, P. (1997). U/Th isotope disequilibria
1100 and ocean island basalt generation in the Azores. *Chemical Geology*, 139(1), 145-164.
1101

1102 Vigouroux, N., Williams-Jones, A. E., Wallace, P., & Staudacher, T. (2009). The
1103 November 2002 eruption of Piton de la Fournaise, Réunion: tracking the pre-eruptive
1104 thermal evolution of magma using melt inclusions. *Bulletin of volcanology*, 71(9), 1077.
1105

1106 Wallace, P. J., Kamenetsky, V. S., & Cervantes, P. (2015). Melt inclusion CO₂ contents,
1107 pressures of olivine crystallization, and the problem of shrinkage bubbles. *American*
1108 *Mineralogist*, 100(4), 787-794.
1109

1110 Walowski, K. J., Wallace, P. J., Hauri, E. H., Wada, I., & Clynne, M. A. (2015). Slab
1111 melting beneath the Cascade Arc driven by dehydration of altered oceanic
1112 peridotite. *Nature Geoscience*, 8(5), 404.

1113 Walowski, K. J., Wallace, P. J., Clyne, M. A., Rasmussen, D. J., & Weis, D. (2016).
1114 Slab melting and magma formation beneath the southern Cascade arc. *Earth and*
1115 *Planetary Science Letters*, 446, 100-112.

1116

1117 Williams, H. M., & Bizimis, M. (2014). Iron isotope tracing of mantle heterogeneity
1118 within the source regions of oceanic basalts. *Earth and Planetary Science Letters*, 404,
1119 396-407.

1120

1121 Workman, R. K., Hart, S. R., Jackson, M., Regelous, M., Farley, K. A., Blusztajn, J., &
1122 Staudigel, H. (2004). Recycled metasomatized lithosphere as the origin of the Enriched
1123 Mantle II (EM2) end-member: Evidence from the Samoan Volcanic
1124 Chain. *Geochemistry, Geophysics, Geosystems*, 5(4).

1125

1126 Witham, F., Blundy, J., Kohn, S. C., Lesne, P., Dixon, J., Churakov, S. V., &
1127 Botcharnikov, R. (2012). SolEx: A model for mixed COHSCI-volatile solubilities and
1128 exsolved gas compositions in basalt. *Computers & Geosciences*, 45, 87-97.

1129

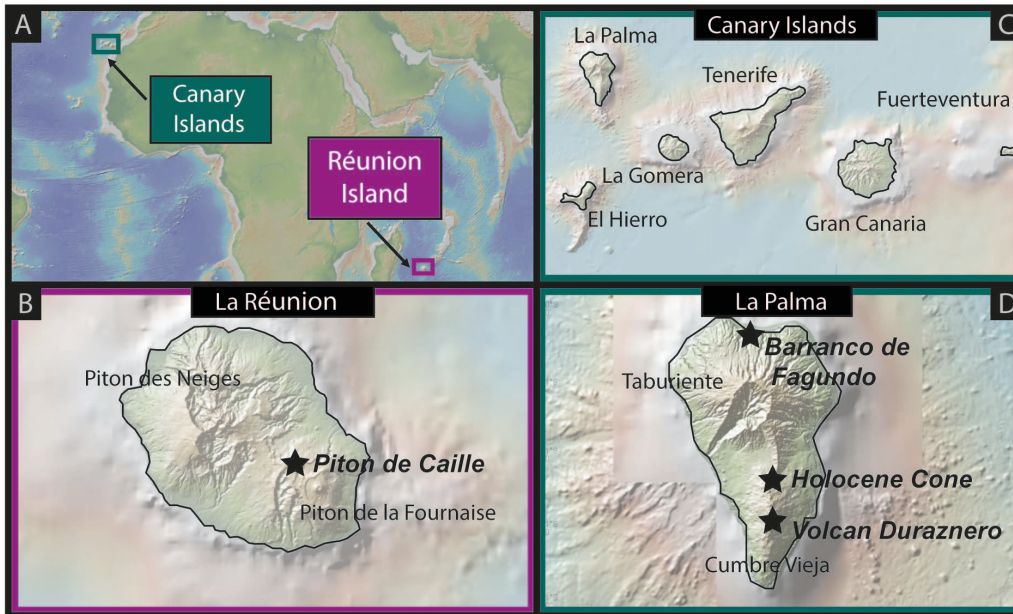
1130 Zindler, A., & Hart, S. (1986). Chemical geodynamics. *Annual review of earth and*
1131 *planetary sciences*, 14(1), 493-571.

1132

1133

1134

1135



1136

1137 Figure 1

1138

1139

1140

1141

1142

1143

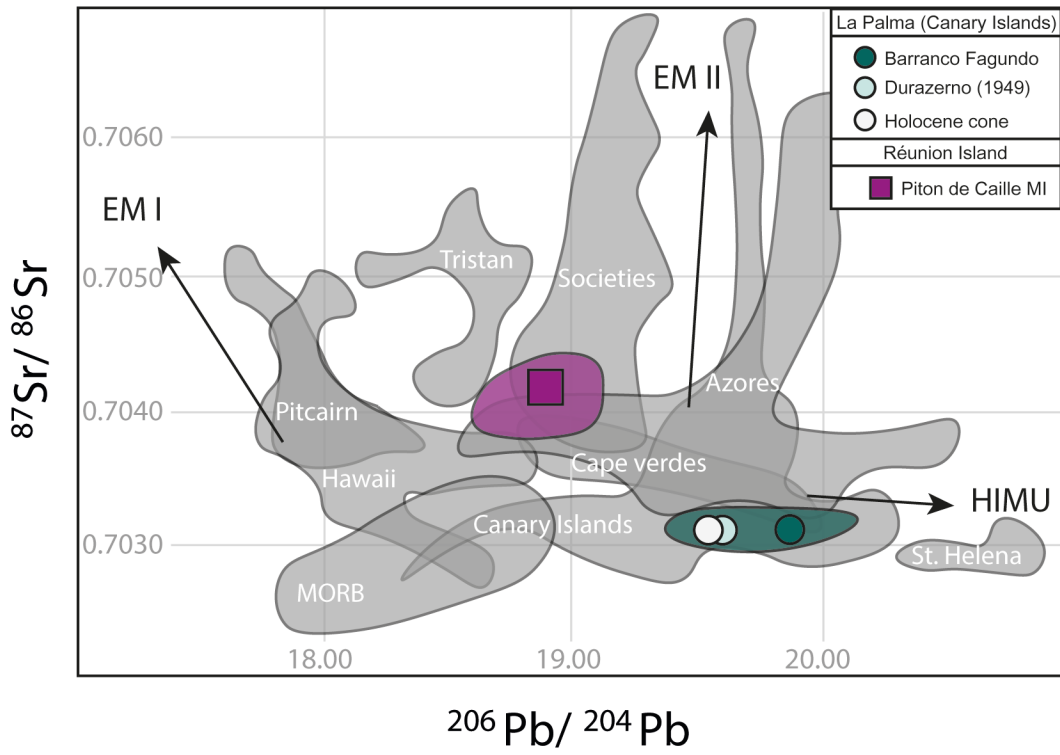
1144

1145

1146

1147

1148



1149

1150 Figure 2

1151

1152

1153

1154

1155

1156

1157

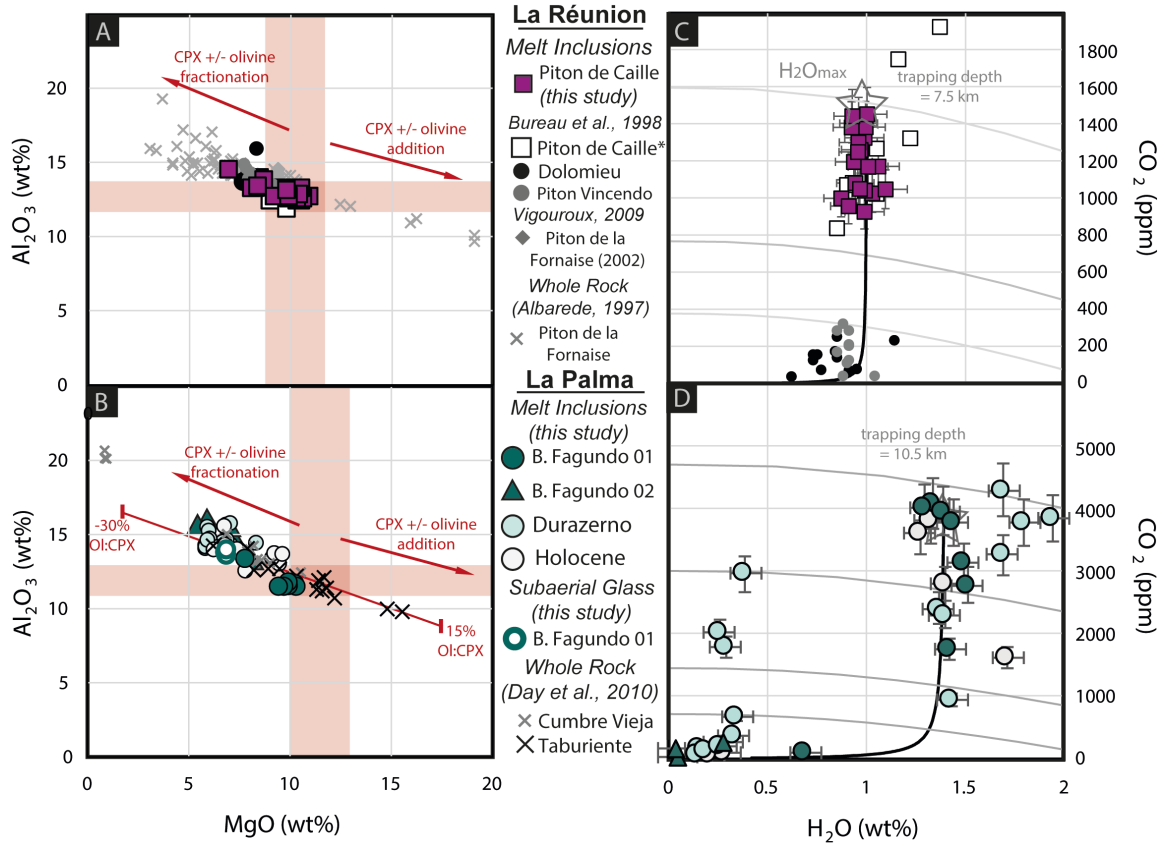
1158

1159

1160

1161

1162



1163

1164 Figure 3

1165

1166

1167

1168

1169

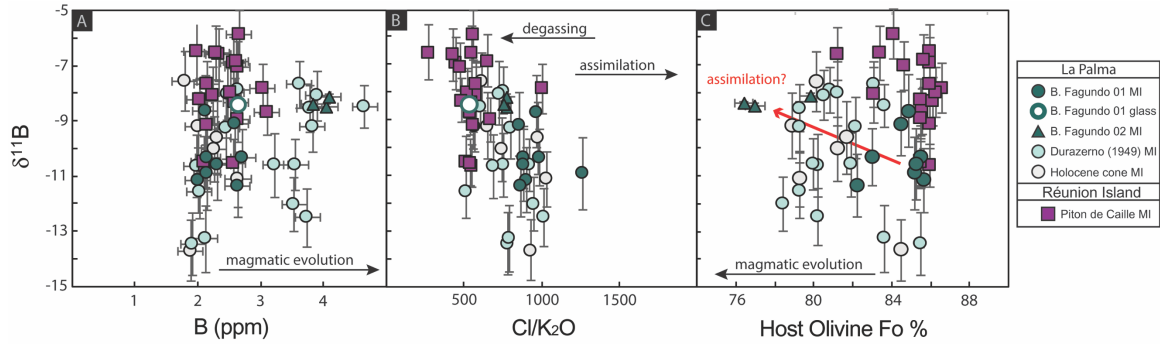
1170

1171

1172

1173

1174



1175

1176 Figure 4

1177

1178

1179

1180

1181

1182

1183

1184

1185

1186

1187

1188

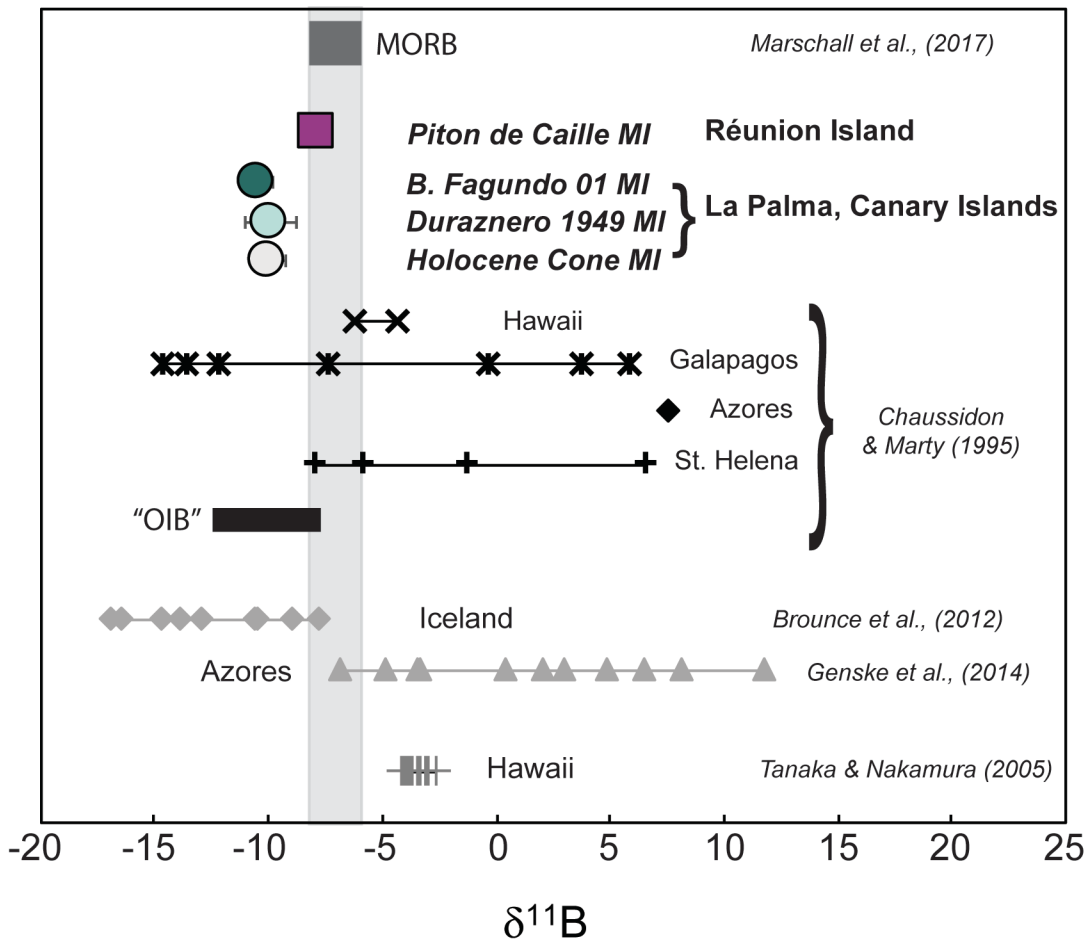
1189

1190

1191

1192

1193



1194

1195 Figure 5

1196

1197

1198

1199

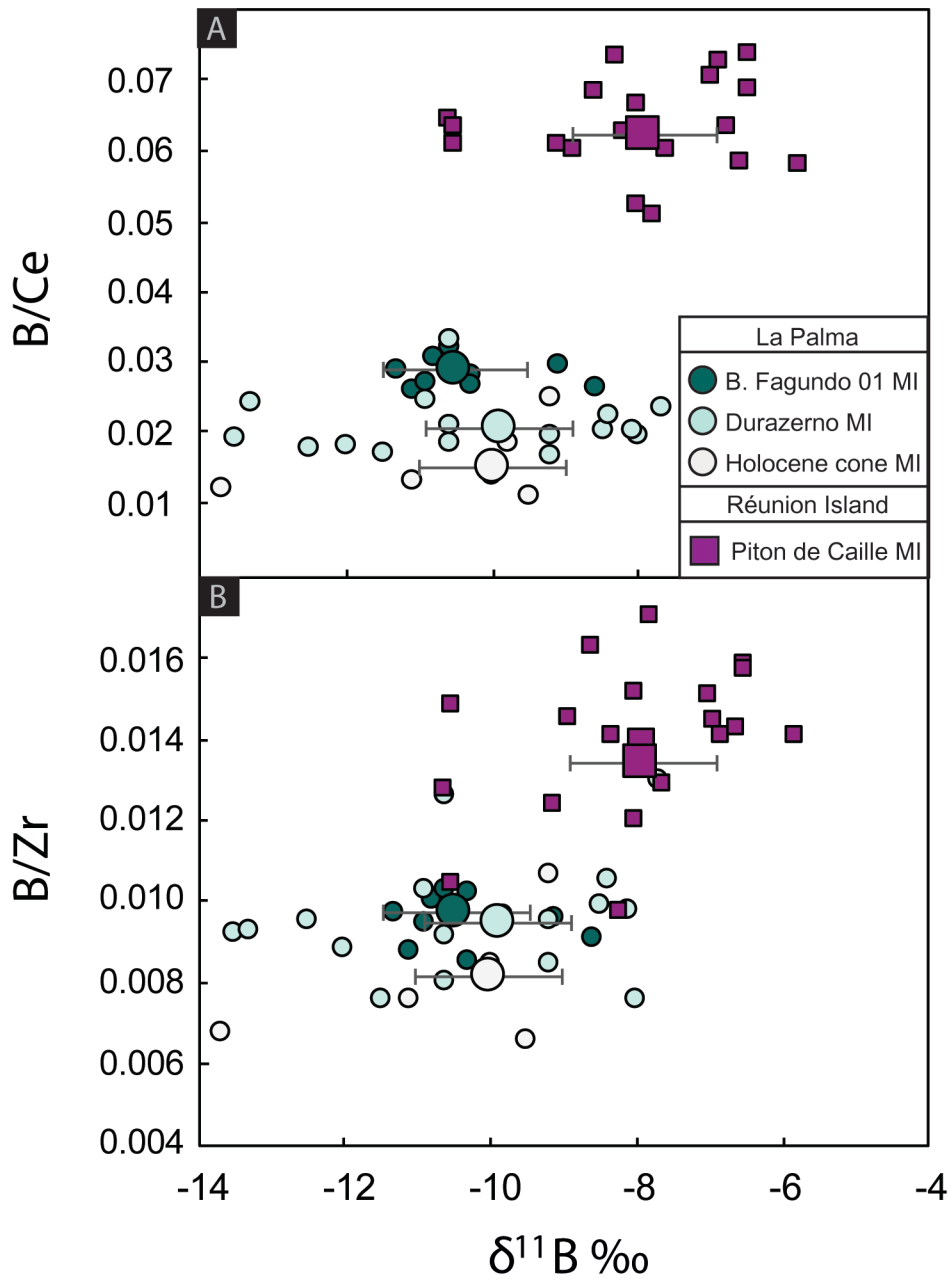
1200

1201

1202

1203

1204



1205

1206 Figure 6

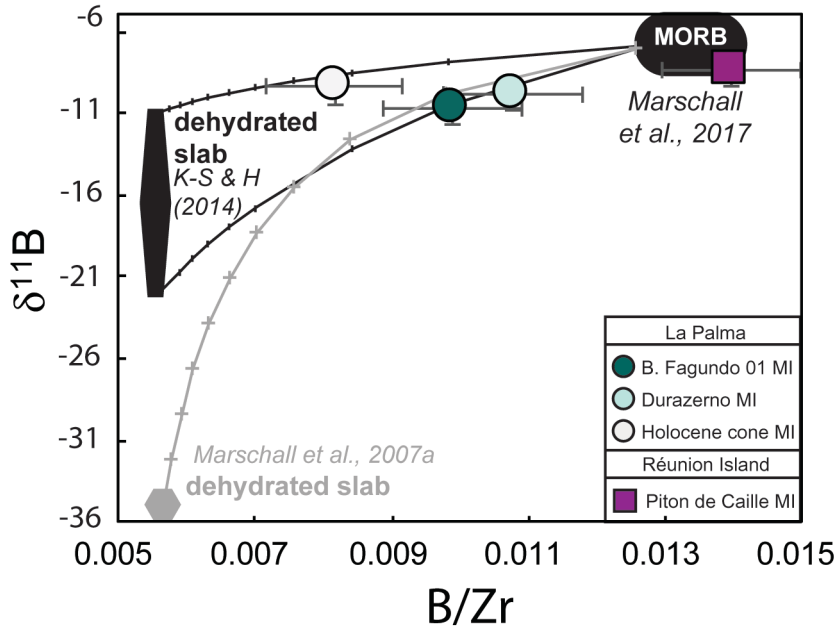
1207

1208

1209

1210

1211



1212

1213 Figure 7

1214

1215

1216

1217

1218

1219

1220

1221

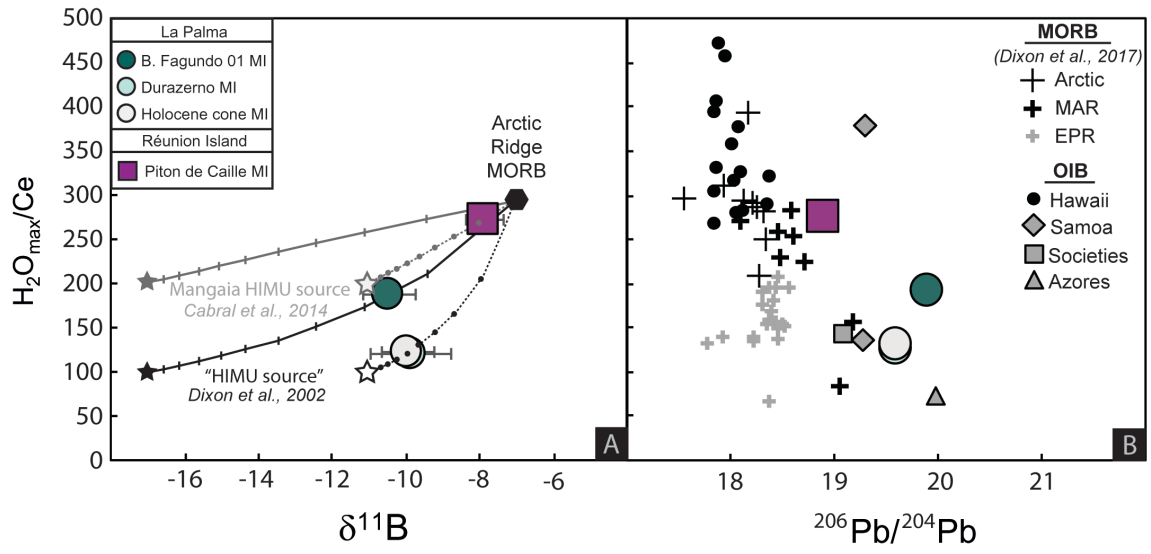
1222

1223

1224

1225

1226



1227

1228 Figure 8

1229